Water Resources Research

RESEARCH ARTICLE
10.1029/2026WR043446

Quasi-Static Pore-Network Modeling for Evaporation-Driven Salt Transport and Precipitation in Porous Media

Zhixin Chen[1], **Bo Guo**[2], **Mathis Kelm**[1], **Theresa Schollenberger**[1], **and Rainer Helmig**[1]

[1]Institute for Modelling Hydraulic and Environmental Systems, University of Stuttgart, Stuttgart, Germany, [2]Department of Hydrology and Atmospheric Sciences, University of Arizona, Tucson, AZ, USA

Key Points:

- We develop a new quasi-static pore-network model to simulate evaporation-driven salt transport and precipitation, accounting for corner flow
- We derive a time-integrated liquid flux approximation during capillary redistribution for efficient modeling of advective salt transport
- The model agrees well with the dynamic pore-network model, with a substantially reduced computational cost

Supporting Information:

Supporting Information may be found in the online version of this article.

Correspondence to:

Z. Chen,
zhixin.chen@iws.uni-stuttgart.de

Citation:

Chen, Z., Guo, B., Kelm, M., Schollenberger, T., & Helmig, R. (2026). Quasi-static pore-network modeling for evaporation-driven salt transport and precipitation in porous media. *Water Resources Research*, *62*, e2026WR043446. https://doi.org/10.1029/2026WR043446

Received 8 JAN 2026
Accepted 8 JUL 2026

Author Contributions:

Conceptualization: Zhixin Chen, Bo Guo, Mathis Kelm, Rainer Helmig
Data curation: Zhixin Chen
Funding acquisition: Bo Guo, Rainer Helmig
Methodology: Zhixin Chen, Bo Guo, Theresa Schollenberger, Rainer Helmig
Project administration: Rainer Helmig
Resources: Rainer Helmig
Software: Zhixin Chen, Mathis Kelm
Supervision: Rainer Helmig
Validation: Zhixin Chen

Abstract Evaporation-driven salt transport and precipitation in porous media involve complex pore-scale processes, where capillary-driven water flow plays a key role in sustaining evaporation and controlling precipitation. Dynamic pore-network models (DPNMs) can resolve these processes but suffer from severe time-step restrictions and high computational costs. Conversely, existing quasi-static models (QSPNMs) are efficient but typically fail to capture solute advection driven by corner flow. We develop a new QSPNM explicitly accounting for corner flow, solute transport, and salt precipitation feedback. The model employs a time-splitting strategy: water vapor and solute diffusion are treated as time-dependent processes, while liquid redistribution and associated advective salt transport are represented as sequences of instantaneous capillary-driven events. Liquid fluxes are approximated using mass conservation and post-redistribution throat conductances, enabling quantitative evaluation of advective solute transport. Diffusive transport of vapor and solute, along with precipitation, is then solved sequentially. The QSPNM is compared against a DPNM for evaporating pure water and brine, yielding volume-weighted spatio-temporal absolute L^2 errors <0.02. For these cases, the QSPNM is approximately one order of magnitude faster than the DPNM using the same time-step size. Because the QSPNM permits substantially larger time steps for comparable accuracy, its computational advantage is expected to increase for general applications. Additional simulations in large three-dimensional pore networks demonstrate the model's capability to simulate domains approaching a representative elementary volume. Overall, the results indicate that the proposed QSPNM captures dominant mechanisms in the capillary-dominated regime, offering a robust and efficient framework for simulating evaporation-driven salt transport and precipitation.

1. Introduction

Evaporation-driven salt precipitation in porous media is a pervasive and complex physicochemical process that compromises the performance and longevity of many critical natural and engineered systems. The adverse impacts span a wide spectrum, including the degradation of salt-affected agricultural soils (Shokri et al., 2024), the decay of porous building materials (Doehne, 2002), potential sequestration capacity impairment in saline aquifer CO_2 storage (Cui et al., 2023), and efficiency losses in solar-driven interfacial desalination (Yang et al., 2024). A key physical process common to all these systems occurs when a brine is exposed to dry air: water removal across the atmosphere–porous media interface induces solute to concentrate at this interface. The ensuing salt transport is a delicate interplay: capillary-driven advection continuously replenishes solute toward the interface, while diffusion drives solute away from high-concentration regions (Bringedal et al., 2022; Chaudhry et al., 2026). Once the local concentration exceeds the solubility limit, salt crystals nucleate and grow, altering the pore geometry and dynamically modifying the coupled hydraulic and transport properties of the porous medium (Jambhekar et al., 2015). These pore-scale alterations necessitate a robust predictive framework to identify the dominant controls on precipitation morphology and to inform effective mitigation strategies (Shokri et al., 2026).

A broad range of numerical models has been developed to analyze this multiphysics problem at both the representative elementary volume (REV) scale (Chaudhry et al., 2026; Guo et al., 2026; Jambhekar et al., 2016; Roy et al., 2022; Wang & Hu, 2023; Zhang et al., 2014) and the pore-scale (Dashtian et al., 2018; Schollenberger et al., 2025; Xiong & Meftah, 2021; Yang et al., 2023). While computationally expedient for laboratory- and field-scale simulations, REV-scale continuum models face several limitations. They rely on volume-averaged parameters and empirical closure relationships (e.g., permeability–porosity functions) that are often difficult to quantify a priori and may insufficiently represent the complexity of the coupled physics (Z. Chen et al., 2025, 2026). By averaging out pore-scale details, these REV-scale models are rendered incapable of resolving discrete,

Writing – original draft: Zhixin Chen
Writing – review & editing: Bo Guo, Mathis Kelm, Theresa Schollenberger, Rainer Helmig

localized phenomena of precipitation, which may be governed by spatial fluctuations in the pore-scale velocity field (Veran-Tissoires & Prat, 2014). These limitations challenge the predictive capabilities of macroscopic advection–diffusion descriptions. Therefore, pore-scale approaches, which explicitly represent the flow dynamics and transport processes within the complex pore geometry, are indispensable. They are essential not only for achieving a mechanistic understanding of pore-scale salt migration and precipitation, but also for developing more robust and physically-based macroscopic formulations to improve REV-scale predictions (Wang et al., 2022, 2025).

Pore-scale salt transport and precipitation can be described using various methods, including pore-network models (PNMs), direct numerical simulations, lattice Boltzmann methods, and phase-field models. Among them, pore-network models offer a compelling alternative by discretizing the void space into pore bodies and throats, providing a computationally efficient framework that preserves essential pore-scale physics. PNMs are broadly classified into two types: QSPNMs and dynamic DPNMs. QSPNMs determine capillary-equilibrium states and recede the air-liquid interface via entry-pressure rules, which neglect viscous forces. In contrast, DPNMs compute the transient evolution of phase distributions and transport by solving coupled mass–momentum conservation equations, thereby accounting for both viscous and capillary forces. In the case of drying porous media, the capillary number (Ca), representing the ratio of viscous to capillary forces, is generally small due to very slow water flow, with typical values often $<10^{-10}$ (Prat, 1993). This indicates that the process is capillarity-dominated, meaning capillary forces almost entirely govern the liquid phase distribution (Lenormand et al., 1988). Therefore, both the QSPNM and the DPNM are expected to be suitable for simulating drying processes.

The development of PNMs to simulate the drying process initially focused on the drying of porous media saturated with pure water. Early efforts employed QSPNMs, which were based on invasion–percolation algorithms modified to include vapor diffusion, as introduced by Nowicki et al. (1992) and Prat (1993). DPNMs were developed later by adapting frameworks from immiscible displacement modeling to the drying process (Yiotis et al., 2004, 2005). This approach was not only able to capture the interplay of viscous and capillary forces but was also essential for resolving the contribution of liquid corner flow to evaporation (Wu et al., 2020). The numerical implementation of DPNMs has continued to evolve, with fully implicit schemes being developed in recent years to ensure mass conservation (S. Chen et al., 2020) and robustly handle the numerically challenging drying dynamics (Weishaupt & Helmig, 2021; Weishaupt et al., 2022; Wu et al., 2023; Schneider et al., 2025). Building on this, Schollenberger et al. (2025) extended the DPNM framework to simulate evaporation in saline systems. Their proposed model couples all the relevant physical processes: two-phase flow, solute advection–diffusion, and precipitation. However, as a general limitation of DPNM, these fully coupled models suffer from significant numerical stability issues due to strong nonlinearities and discontinuities (e.g., Haines jumps). This leads to convergence challenges and requires extremely small time steps (Schneider et al., 2025). Consequently, they are often computationally infeasible for the slow, long-duration processes typical of evaporation-driven salt precipitation with large pore network structures. At the same time, recent pore-scale experiments have provided strong physical support for the crucial role of corner liquid flow during evaporation. For pure-water systems, microfluidic experiments, together with corresponding pore-network analyses, have shown not only that corner films can be directly observed, but also that accounting for both continuous and discontinuous corner flow is essential for quantitatively reproducing pore-scale liquid redistribution and evaporation kinetics (Prat, 2007; Wu et al., 2020). For saline systems, recent visualization studies have likewise provided direct evidence for the presence and importance of corner liquid films in dissolved-salt transport, salt precipitation, and air–liquid displacement (Wu & Chen, 2023; Zhang et al., 2024). However, evaporation-driven salt precipitation involves more strongly coupled pore-scale processes and is highly sensitive to experimental conditions, including wettability, evaporation rate, pore geometry, and liquid connectivity. As a result, while the physical relevance of corner liquid flow in saline systems is now well supported qualitatively, systematic quantitative experiment-to-model validation remains much more limited than in pure-water drying.

Parallel to the development of DPNMs, QSPNMs have also been extended to brine systems by incorporating solute advection–diffusion and precipitation (Ahmad et al., 2021; Dashtian et al., 2018; Veran-Tissoires & Prat, 2014). By sequentially calculating vapor diffusion, liquid transport, solute transport, and precipitation, this approach was intended to be more computationally efficient than DPNMs. However, current QSPNMs for evaporation-driven salt precipitation still exhibit significant limitations. First, corner flow is typically neglected in

existing QSPNMs for brine systems. These models generally assume that pore throats are perfectly circular and become completely dry upon gas invasion (Dashtian et al., 2018). Consequently, the residual liquid residing in the corners of invaded throats is ignored, and solute transport is unrealistically confined to the fully saturated bulk clusters. This structural simplification prevents these models from capturing an important transport pathway: salt migration from the interior of the porous medium to the evaporative surface through continuous corner liquid. Second, classical QSPNMs inherently lack transient liquid-phase fluxes because liquid redistribution is determined from a sequence of static capillary-equilibrium states rather than a dynamic flow solution (Wu et al., 2020). To approximate advective transport, previous QSPNMs impose a steady-state liquid redistribution calculation between two discrete gas invasion events (Ahmad et al., 2021; Dashtian et al., 2018). Although vapor diffusion drives evaporation across all exposed throats at the drying front, these models assume that only the largest throat at the drying front actively drains. The liquid displaced from this newly invaded throat is then redistributed through the connected liquid cluster by capillary pumping, that is, the capillary-pressure-driven flow from larger drained throats toward the finer interfacial throats whose menisci sustain higher capillary suction (Lehmann et al., 2008). This redistribution compensates for the evaporative losses at the remaining interfacial throats. The corresponding liquid fluxes are computed assuming Hagen–Poiseuille-type flow. However, this treatment introduces a spatially varying liquid-pressure field within the cluster. Because gas-pressure gradients are neglected, these liquid-pressure variations imply different capillary pressures at different interfacial menisci, which is inconsistent with the capillary-equilibrium assumption underlying the quasi-static formulation. This limitation becomes even more critical when corner flow is considered. The previous flux calculation strategy relies on the premise that an invaded throat is excluded from the liquid flow network and no longer participates in liquid transport. Such a premise is no longer valid when liquid remains hydraulically connected through the corners of invaded throats. In that case, liquid continuity extends not only through bulk uninvaded clusters but also through corner liquid in invaded regions, enabling salt transport throughout the entire connected liquid phase. Consequently, the previous flux-calculation strategy, which restricts drainage to the single largest interfacial throat and resolves the remaining liquid pressures from Hagen–Poiseuille flow inside the bulk-saturated cluster, no longer suffices when corner flow is present. Liquid fluxes must then be resolved over the entire connected liquid phase, including the corner films in invaded throats, both during the slow drying intervals between invasions and at the discrete invasion events themselves.

The objective of the present study is to develop a new QSPNM that captures the key pore-scale physics of evaporation-driven salt transport and precipitation in porous media at the capillary-dominated regime, while remaining sufficiently computationally efficient to enable systematic parameter studies on large pore network structures. The proposed QSPNM framework incorporates advective salt transport via corner flow to address the critical limitations of existing models. A time-integrated liquid flux approximation is derived for flow within the interconnected liquid phase, providing the advective fluxes required to model coupled advective–diffusive salt transport and precipitation. The QSPNM framework is then compared against a fully implicit DPNM (Schollenberger et al., 2025) using several benchmark cases for both pure water and brine evaporation. The advantages of the proposed framework in terms of numerical convergence and computational efficiency are also quantified by the comparison of the two models. Finally, we demonstrate the enhanced computational capability of the QSPNM by applying it to a larger-scale pore network, illustrating its potential for simulating realistic porous media where dynamic models may be computationally prohibitive.

2. Quasi-Static Pore-Network Modeling Framework

We develop a quasi-static pore-scale modeling framework to simulate the various transport and precipitation processes of salt in porous media driven by isothermal evaporation, explicitly accounting for corner flow. This framework is built upon the principles of QSPNMs that have been used for the pore-scale simulation of drying of pure or saline water (Ahmad et al., 2021; Biswas et al., 2018; Dashtian et al., 2018; Nowicki et al., 1992; Prat, 1993; Schollenberger et al., 2025; Surasani et al., 2010). In this section, we first introduce the pore network representation and then define the simulation regime of our proposed framework. Based on this, we present the mathematical formulations governing the pore-scale processes: the drying process, unsaturated flow (including liquid film flow), salt transport, and salt precipitation. Finally, we outline the computational algorithm of the proposed framework.

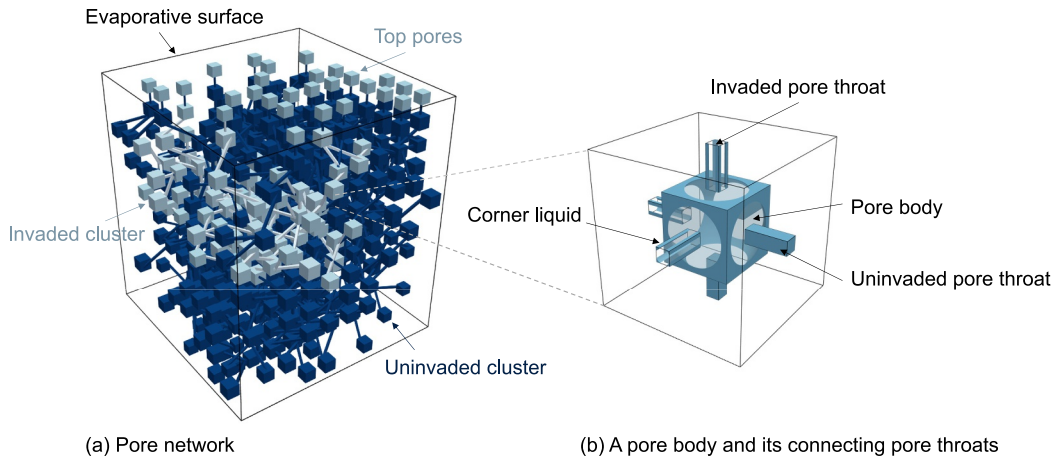

Figure 1. (a) An example of 3D pore network during the simulation of evaporation-driven salt transport and precipitation, (b) a zoomed-in view of an invaded pore body and its connecting pore throats.

2.1. Pore Network Representation

To analyze the main processes of evaporation-driven salt transport and precipitation, we represent the pore structure of a porous medium as a pore network, which can be constructed using a network generation algorithm (e.g., Weishaupt and Helmig (2021)). Figure 1a illustrates a 3D pore network during the simulation of evaporation-driven salt transport and precipitation. We discretize the void volume of the porous medium into pore bodies, represented as cubes, as shown in Figure 1b. The radius of each pore body is defined by the radius of the inscribed sphere of the cube. After a pore body is invaded, liquid may exist in the corners and on the walls of the invaded pore body.

The pore bodies are interconnected by pore throats with a square cross-section, which allow for corner flow along their four corner edges when invaded (see Figure 1b). The pore throats are assumed to be volumeless and serve only to provide hydraulic conductance for bulk liquid and liquid film flow. The pore throat radius is defined as the inscribed circle radius of the square cross-section and is determined based on the neighboring pore bodies (Joekar-Niasar et al., 2008). In pore-network models, pore bodies are commonly idealized as spheres or cubes (Joekar-Niasar et al., 2008), while pore throats are commonly represented as channels with circular, square, or triangular cross-sections (Joekar-Niasar et al., 2008; Patzek & Silin, 2001; Øren et al., 1998). A key distinction among these idealized shapes is that angular cross-sections (e.g., square and triangular) permit the formation of wetting layers in the corners of invaded throats, thereby maintaining hydraulic connectivity through corner liquid. In contrast, circular cross-sections do not possess corners and cannot sustain such corner liquid. Since corner flow is a prerequisite for modeling the coupled salt transport processes in the present work, it is critical to employ an angular cross-section. Among angular geometries, we adopt cubic pore bodies and square-cross-section pore throats, following common practice in PNM studies (S. Chen et al., 2020; Joekar-Niasar et al., 2008). This choice also ensures geometric consistency with the DPNM of Schollenberger et al. (2025), against which the proposed QSPNM is verified in Section 4. We note that the proposed framework is not restricted to this specific geometry. The local rules governing capillary pressure, entry pressure, and hydraulic conductance (Section 2.8) are formulated in a modular manner and can be adapted for other angular cross-sectional shapes.

The set of invaded pores is denoted as the invaded cluster, while the set of uninvaded pores is denoted as the uninvaded cluster. Detailed information on the geometric parameters and boundary conditions of the pore networks used in the benchmark cases will be given in Section 3.

2.2. Capillary-Dominated Regime

We define the simulation regime of our proposed framework as the capillary-dominated regime, which is characterized by a small *Ca* value. *Ca* is defined as the ratio of viscous to capillary forces, given by:

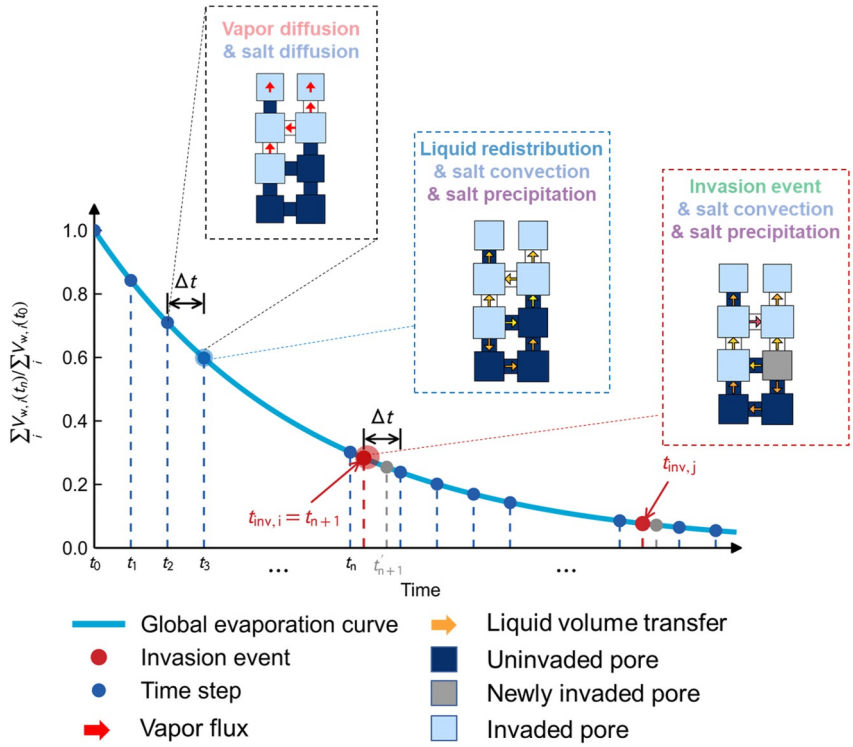

Figure 2. Schematic figure of QSPNM framework for simulation of evaporation-driven salt transport and precipitation.

$$Ca = \frac{\mu_w q_e}{A_e \sigma}, \tag{1}$$

where μ_w is the dynamic viscosity of the liquid, q_e is the evaporation flux at the evaporative surface (see Figure 1), A_e is the surface area of the evaporative surface, and σ is the surface tension of the liquid. Under this condition, the liquid flow is governed by capillary forces and the drying process is sufficiently slow to be treated as isothermal.

Furthermore, within the capillary-dominated regime, the time scale of vapor diffusion is much longer than that of liquid flow during the drying of porous media (Borgman et al., 2017). This time-scale separation motivates a quasi-static approach, where we represent the evolution of the liquid phase distribution as a sequence of capillary equilibrium configurations, while treating vapor and salt diffusion as slow, time-dependent processes.

To implement this approach, we discretize the process into time steps Δt and apply a time-splitting strategy, as schematically shown in Figure 2a. Within each time step, a trial update is first performed over the full interval $[t_n, t_{n+1}]$, including vapor diffusion in the gas phase, drying-induced liquid redistribution, the associated advective salt transport, and salt diffusion in the liquid phase. Based on the resulting predicted capillary state, we then check whether an invasion event occurs within the current time step. If no invasion is triggered, salt precipitation/dissolution and the associated pore-space alteration are applied over Δt. If an invasion is triggered, the invasion time t_{inv} is localized within $(t_n, t_{n+1}]$, the system state is rolled back to t_n, and the trial update is recomputed only over the subinterval $[t_n, t_{\text{inv}}]$. The invasion event is then executed, followed by invasion-induced redistribution and the corresponding advective salt transport. Salt precipitation/dissolution and geometry update are finally applied using the actual advanced time interval. This time-splitting scheme effectively decouples the slow transport processes from the fast capillary-driven processes while preserving the correct invasion sequence.

Based on this strategy, the modeling is decomposed into several sub-processes: vapor diffusion in the gas phase (Section 2.3), percolation-based liquid redistribution (Section 2.4), time-integrated liquid-flux approximation for advective salt transport (Section 2.5), salt transport via advection and diffusion (Section 2.6), invasion-event localization and update (Section 2.4), and salt precipitation with pore-space alteration (Section 2.7).

2.3. Vapor Diffusion in Gas Phase

In the pore network, we set the side and bottom boundaries as impermeable and the top boundary as the evaporative surface, as illustrated in Figure 1. This configuration is widely adopted in PNMs for drying (Borgman et al., 2017; Prat, 1993; Schollenberger et al., 2025; Wu & Zhao, 2021; Yiotis et al., 2007). As a result, vapor transport out of the network takes place via a diffusive boundary layer between the atmosphere and the top pore bodies.

The driving force for drying is the gradient of vapor concentration. The diffusive flux of water vapor from a top pore body i to the ambient atmosphere, $J^{w}_{\mathrm{diff,amb},i}$, is given by:

$$J^{w}_{\mathrm{diff,amb},i} = -D^{w,a}_{g}\frac{x^{w}_{g,i}\rho_{\mathrm{mol},g,i} - x^{w}_{g,\,\mathrm{amb}}\rho_{\mathrm{mol},g,\mathrm{amb}}}{\delta}, \tag{2}$$

where $\rho_{\mathrm{mol},g,i}$ and $\rho_{\mathrm{mol},g,\mathrm{amb}}$ are the gas molar densities at the top pore body i and in the ambient atmosphere, respectively, $D^{w,a}_{g}$ is the diffusion coefficient of water vapor in the gas phase, $x^{w}_{g,i}$ is the vapor mole fraction at the top pore body i, $x^{w}_{g,\,\mathrm{amb}}$ is the ambient vapor mole fraction (in the atmosphere), and δ is the thickness of the diffusive boundary layer. The total molar flow rate from pore i is then $J^{w}_{\mathrm{diff,amb},i}A_i$, where A_i is the surface area of the top pore body i.

As evaporation proceeds, gas invades the initially saturated pore network. Liquid-saturated pore bodies become unsaturated once one of their connecting pore throats is invaded. Because liquid flow persists along the corners of invaded pore bodies and throats, the invaded cluster remains hydraulically connected, so that each invaded pore body remains unsaturated rather than fully dry during the drying process, as long as the corner liquid keeps neighboring pore bodies connected. When the local capillary pressure in a pore body exceeds the disconnection threshold $p^{\mathrm{thr}}_{c,i}$ introduced in Section 2.8.3, the corner liquid in that pore body loses its hydraulic connection to its neighbors, and the invaded cluster may split into several hydraulically independent sub-clusters. Each isolated sub-cluster still exchanges water vapor with the surrounding gas phase through its invaded pore throats, so evaporation and, in the brine case, salt accumulation and precipitation continue inside these isolated sub-clusters; they, however, no longer receive liquid compensation through capillary pumping from other parts of the network.

Therefore, assuming gas-liquid equilibrium at each pore body, the vapor concentration at the invaded pore bodies is determined by the salt concentration, as described by Raoult's law:

$$x^{w}_{g,i} = x^{w,\mathrm{sat}}_{g}\left(1 - x^{\mathrm{salt}}_{w,i}\right), \tag{3}$$

where $x^{w}_{g,i}$ is the vapor mole fraction at the invaded pore body i, $x^{w,\mathrm{sat}}_{g}$ is the saturated vapor mole fraction, and $x^{\mathrm{salt}}_{w,i}$ is the liquid mole fraction of salt at the invaded pore body i.

The diffusion flux of vapor $J^{w}_{\mathrm{diff},g,ij}$ between pore bodies i and j within the invaded cluster is given by Fick's law:

$$J^{w}_{\mathrm{diff},g,ij} = -D^{w,\mathrm{a}}_{g}\frac{x^{w}_{g,i}\rho_{\mathrm{mol},g,i} - x^{w}_{g,j}\rho_{\mathrm{mol},g,j}}{l_{ij}}, \tag{4}$$

where $\rho_{\mathrm{mol},g,i}$ and $\rho_{\mathrm{mol},g,j}$ are the gas molar densities at pore bodies i and j, respectively, and l_{ij} is the length of the pore throat ij, defined as the distance between the two pore body centers minus the sum of the radii of the two pore bodies. The mass conservation equation for water vapor in each pore body i within the invaded cluster is then established as:

$$\sum_{j} J^{w}_{\mathrm{diff},g,ij}A_{g,ij} + Q^{w}_{g\to w,i} = 0, \tag{5}$$

where $A_{g,ij}$ is the gas phase cross-section area of the pore throat ij. $Q^{w}_{g\to w,i}$ is the molar rate of phase change (evaporation/condensation) at the liquid interface within pore i. This sink/source term $Q^{w}_{g\to w,i}$ is then used to update the liquid saturation and salt concentration in the pore body.

Specifically, the update of liquid saturation and salt concentration from $Q^{w}_{g\to w,i}$ proceeds as follows. Let t_n and $t_{n+1} = t_n + \Delta t$ denote the beginning and end of a time step, respectively. We denote the moles of water and dissolved salt in pore body i by $n_{w,i}$ and $n_{s,i}$, respectively. Since only water undergoes phase change, the dissolved salt content is strictly conserved during vapor diffusion:

$$n_{s,i}^{t_{n+1}} = n_{s,i}^{t_n}. \tag{6}$$

The water content is updated from the phase change rate obtained via Equation 5:

$$n_{w,i}^{t_{n+1}} = n_{w,i}^{t_n} + Q^{w}_{g\to w,i}\,\Delta t. \tag{7}$$

The salt mole fraction is then recalculated from the updated composition:

$$x_{w,i}^{\mathrm{salt},\,t_{n+1}} = \frac{n_{s,i}^{t_{n+1}}}{n_{w,i}^{t_{n+1}} + n_{s,i}^{t_{n+1}}}. \tag{8}$$

The liquid molar density is then evaluated from the brine equation of state at the updated composition, that is, $\rho_{\mathrm{mol},w,i}^{t_{n+1}} = \rho_{\mathrm{mol}w,}\left(x_{w,i}^{\mathrm{salt},\,t_{n+1}}\right)$. The liquid volume and saturation are subsequently updated as:

$$V_{w,i}^{t_{n+1}} = \frac{n_{w,i}^{t_{n+1}} + n_{s,i}^{t_{n+1}}}{\rho_{\mathrm{mol},w,i}^{t_{n+1}}}, \qquad S_{w,i}^{t_{n+1}} = \frac{V_{w,i}^{t_{n+1}}}{V_i}. \tag{9}$$

This procedure ensures local conservation of both water and dissolved salt during each time step. A similar update of these variables is applied after salt diffusion (Section 2.6.2): when diffusive transport changes the dissolved salt content in each pore body, the updated salt mole fraction, liquid molar density, and liquid saturation are recalculated self-consistently using Equations 8 and 9.

2.4. Percolation Process in Liquid Phase

As mentioned above, we represent the evolution of the liquid-phase distribution as a sequence of equilibrium configurations. Traditional QSPNMs only update the liquid phase distribution after an invasion event, as they assume the pore throat is fully hydraulically disconnected from the bulk liquid once invaded. However, as we described in Section 2.1, our model includes corner liquid, which ensures the invaded cluster remains internally hydraulically connected. Therefore, the liquid phase distribution in the invaded cluster should be updated instantaneously via percolation theory at the end of each time step (not just after an invasion event).

This redistribution is necessary to establish a new capillary equilibrium, as evaporation (calculated in Section 2.3) has removed liquid mass from the cluster, which induces a capillary pressure difference within the invaded cluster at the end of each time step.

We denote the state of the pore network before this capillary redistribution as Γ_b (the non-equilibrium state after mass loss) and the state after as Γ_f (the new equilibrium state). The redistribution is solved by enforcing mass conservation, which states that the total liquid mass in the new equilibrium state Γ_f must equal the known mass in the state Γ_b. This is formulated as a nonlinear problem for the unknown global capillary pressure $p_{c,C_k}^{\Gamma_f}$:

$$\begin{cases} \displaystyle\sum_{i\in C_k} S_{w,i}^{\Gamma_b}\left(p_{c,C_k}^{\Gamma_b}, r_i\right) V_i = \sum_{i\in C_k} S_{w,i}^{\Gamma_f}\left(p_{c,C_k}^{\Gamma_f}, r_i\right) V_i \\ p_{c,i}^{\Gamma_f} = p_{c,C_k}^{\Gamma_f}, \quad \forall\, i \in C_k \end{cases} \tag{10}$$

where $S_{w,i}^{\Gamma_b}$ is the known liquid saturation of pore i in the state Γ_b (i.e., after mass loss from evaporation), V_i is the volume of pore i, r_i is the radius of pore body i, and $p_{c,C_k}^{\Gamma_f}$ is the unknown global capillary pressure of the cluster C_k

in the final equilibrium state Γ_f. Once $p_{c,C_k}^{\Gamma_f}$ is determined, the liquid saturation of each pore in the invaded cluster can be calculated using Equation 33.

In addition to this redistribution from drying, the continuous increase in capillary pressure can also trigger an invasion event. This event happens when the cluster capillary pressure p_{c,C_k} rises to meet the entry pressure of an adjacent uninvaded throat. Following the principles of invasion percolation, the first throat to be invaded will be the one with the minimum capillary entry pressure among all throats τ attached to the currently invaded cluster C_k. We denote this set of available throats by $\mathcal{T}_{\text{uninv}}(C_k)$ and define this minimum entry pressure as:

$$p_{c,\min}^{\text{entry}} = \min_{\tau \in \mathcal{T}_{\text{uninv}}(C_k)} p_{c,\text{entry}}(\tau). \tag{11}$$

During a time step $[t_n, t_{n+1}]$, a trial update is first performed over the full interval, including vapor diffusion, drying-induced liquid redistribution, the corresponding advective salt transport, and salt diffusion, as illustrated in Figure 2. Based on the resulting predicted capillary state, invasion is treated as a discrete event that may occur within the time step. Accordingly, the cluster capillary pressure p_{c,C_k} advances from $p_{c,C_k}^{t_n}$ to $p_{c,C_k}^{t_{n+1}}$. An invasion occurs within this time step if:

$$p_{c,C_k}^{t_n} < p_{c,\min}^{\text{entry}} \le p_{c,C_k}^{t_{n+1}}. \tag{12}$$

If Equation 12 is satisfied, it is necessary to locate the invasion time t_{inv} inside $(t_n, t_{n+1}]$, rather than simply assigning the invasion to t_{n+1}. This event localization is essential for correctly identifying the invasion sequence and the corresponding redistribution state before updating the subsequent advective salt transport. In practice, once t_{inv} is found, the state is rolled back to t_n and the trial update is recomputed only over $[t_n, t_{\text{inv}}]$. More importantly, this treatment enables the proposed QSPNM to avoid resolving the fast invasion dynamics with extremely small time steps, which is one of the key reasons why the method can remain accurate while permitting significantly larger time steps than traditional DPNMs.

To locate the invasion time $t_{\text{inv}} \in (t_n, t_{n+1}]$, let $\tau_\star \in \mathcal{T}_{\text{uninv}}(C_k)$ be the pore throat attaining $p_{c,\min}^{\text{entry}}$, and let i be an uninvaded pore body adjacent to $\tau_\star$. We determine this pore body's liquid saturation $S_{w,i}(t)$ by linear interpolation:

$$S_{w,i}(t) = S_{w,i}^{t_n} + \theta\left(S_{w,i}^{t_{n+1}} - S_{w,i}^{t_n}\right), \qquad \theta := \frac{t - t_n}{\Delta t} \in [0,1], \quad \Delta t := t_{n+1} - t_n. \tag{13}$$

Let $p_{c,i}(t) := p_c(S_{w,i}(t))$ be the capillary pressure in pore i, evaluated via the constitutive relation (Equation 33). t_{inv} is then defined as the root of the following equation:

$$f_{i,\tau_\star}(t) := p_{c,i}(t) - p_{c,\text{entry}}(\tau_\star) = 0, \qquad t \in (t_n, t_{n+1}], \tag{14}$$

which exists and is unique under the monotonicity of Equation 33.

Once t_{inv} is found, the state is first rolled back to t_n, and the evolution over the current time step is recomputed only over the subinterval $[t_n, t_{\text{inv}}]$. In this way, the liquid saturation and capillary state immediately before invasion are determined consistently at t_{inv}. The newly invaded pore and newly invaded throat (i.e., $\tau_\star$) are then added to the invaded cluster, which is denoted as $C_k^{t_{\text{inv}}}$. As the newly invaded pore transitions from saturated to unsaturated, its liquid mass is released, triggering a redistribution throughout the entire updated cluster $C_k^{t_{\text{inv}}}$ to reach a new capillary equilibrium. We denote the state immediately before this liquid is released as Γ_b, and the final equilibrium state reached after this redistribution as Γ_f. The new liquid distribution (at state Γ_f) is then obtained by solving the mass-conservation system, as described in Equation 10.

2.5. Time-Integrated Liquid Flux During Redistribution Events

A DPNM can solve the transient two-phase flow for evaporation-driven salt transport and precipitation with fully implicit schemes, explicitly obtaining the flux of liquid phase at each time step. In contrast, a QSPNM updates liquid phase distribution instantaneously via the percolation theory at the end of each time step or after each

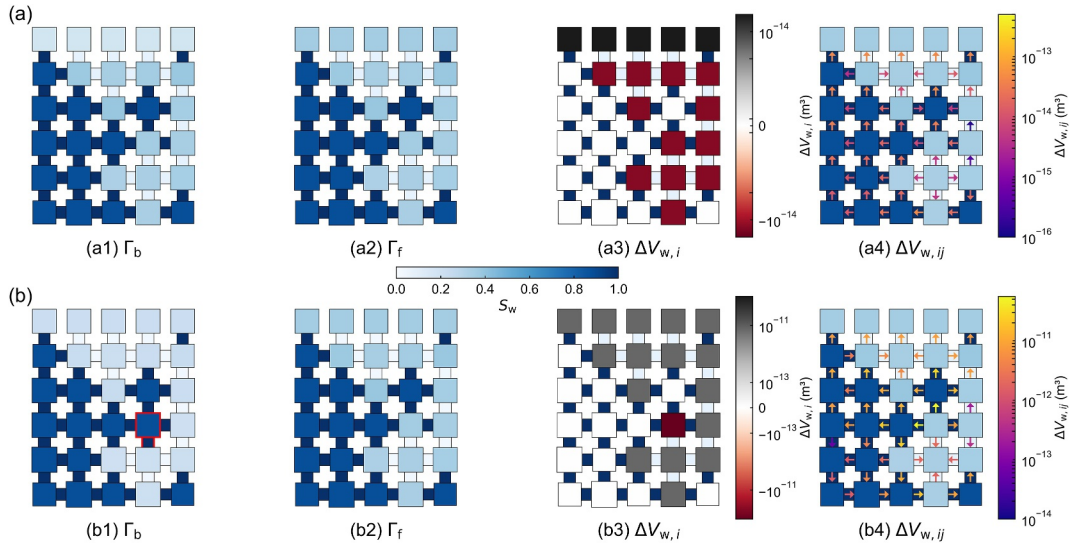

Figure 3. Schematic figure of liquid flux approximation during (a) drying-induced redistribution and (b) invasion-induced redistribution.

invasion event. Since this instantaneous redistribution is not resolved as a transient process, the liquid fluxes during this redistribution are not computed. However, this information is essential for solving the advective transport of salt in the liquid phase. To overcome this limitation, we propose a method to estimate the time-integrated liquid fluxes within the network during this redistribution process.

The physical basis of this method is illustrated in Figure 3. In the case of drying-induced redistribution (Figure 3a3), multiple top pore bodies simultaneously lose liquid due to evaporation before redistribution and are replenished by the remaining liquid in the invaded cluster after redistribution. For the invasion-induced redistribution (Figure 3b3), the newly invaded pore (highlighted in the red rectangle in Figure 3b1) displaces liquid into the connected invaded cluster after redistribution. Although Figure 3b depicts a single newly invaded pore, an invasion event may involve multiple newly invaded pores simultaneously, depending on the number of the largest pore throats that are connected to the invaded cluster. Regardless of the number of newly invaded pores, the fundamental mechanism of the redistribution remains unchanged, as it involves simultaneous liquid displacement from multiple invaded pore bodies. This process is physically analogous to the simultaneous liquid loss occurring during drying-induced redistribution.

We denote the state of the pore-network model before and after redistribution (induced by either invasion or drying) as Γ_b and Γ_f, respectively. Although the redistribution is assumed to be instantaneous, we mathematically resolve it over an infinitesimal time interval δt. The throat conductances, $g_{w,ij}^{\Gamma_b}$ and $g_{w,ij}^{\Gamma_f}$, are determined by the relationship described in Equation 37. The time-integrated liquid flux $\Delta V_{w,ij}$ through pore throat ij is defined by the integral of the instantaneous flow rate over this infinitesimal interval:

$$\Delta V_{w,ij} = \int_t^{t+\delta t} q_{w,ij}(t)\,\mathrm{d}t, \tag{15}$$

where the liquid flux $q_{w,ij}(t)$ is determined by

$$q_{w,ij}(t) = g_{w,ij}^{\Gamma(t)}\left(p_{w,i}(t) - p_{w,j}(t)\right), \tag{16}$$

where $p_{w,i}$ and $p_{w,j}$ are the liquid phase pressures in pore bodies i and j, respectively.

Given that δt is infinitesimal, we can approximate this time-integrated flux using a time-averaged pressure field:

$$\Delta V_{w,ij} \approx g_{w,ij}^{\Gamma_*}\left(\bar{p}_{w,i} - \bar{p}_{w,j}\right)\delta t, \qquad \bar{p}_{w,i} := \frac{1}{\delta t}\int_t^{t+\delta t} p_{w,i}(t)\,\mathrm{d}t, \tag{17}$$

where $g_{w,ij}^{\Gamma_*}$ is a representative conductance (e.g., $g_{w,ij}^{\Gamma_b}$, $g_{w,ij}^{\Gamma_f}$, or their harmonic mean $g_{w,ij}^{\Gamma_{\mathrm{hm}}}$). Furthermore, the liquid volume change $\Delta V_{w,i}$ at each pore i before and after the redistribution can be obtained from the saturation change:

$$\Delta V_{w,i} = V_i\left(S_{w,i}^{\Gamma_f} - S_{w,i}^{\Gamma_b}\right). \tag{18}$$

Enforcing mass conservation at each pore body i, where $\mathcal{N}(i)$ is the set of its neighboring pore bodies, requires that the net liquid transfer from its neighbors equals the nodal liquid volume change:

$$\sum_{j\in\mathcal{N}(i)} \Delta V_{w,ij} = \Delta V_{w,i}. \tag{19}$$

Substituting our approximation (Equation 17), we obtain the following linear system for the unknown average pressures:

$$\delta t \sum_{j\in\mathcal{N}(i)} g_{w,ij}^{\Gamma_*}\left(\bar{p}_{w,i} - \bar{p}_{w,j}\right) = \Delta V_{w,i}. \tag{20}$$

To solve this linear system, we fix one reference pore (e.g., set $\bar{p}_{w,0} = 0$) to ensure a unique solution. Because the fluxes are driven by the pressure gradient, the results do not depend on which pore is selected as the reference. The resulting average pressure differences $\bar{\boldsymbol{p}}_w$ that drive the instantaneous redistribution of the liquid phase can then be computed. Moreover, since $\bar{\boldsymbol{p}}_w$ scales inversely with δt, $\Delta V_{w,ij}$ in each throat is invariant with respect to the choice of δt. Consequently, a unique and well-defined solution for $\Delta V_{w,ij}$ can be obtained. This method yields a physically consistent approximation of time-integrated liquid fluxes that matches the prescribed porewise volume changes implied by $\{\Gamma_b, \Gamma_f\}$ while enforcing instantaneous hydrostatic compatibility across the pore network. The calculated $\Delta V_{w,ij}$ can then be used to calculate the advective transport of salt in the liquid phase.

2.6. Modeling of Salt Transport in a Pore Network

Salt transport in the liquid phase is governed by advective and diffusive processes. We track the salt concentration at each pore i, assuming a spatially uniform (well-mixed) state. Advective transport is driven by the liquid volume transport, while diffusive transport is driven by concentration gradients. Both processes are solved using an implicit time scheme, as described below.

2.6.1. Advection of Dissolved Salt

Advection of dissolved salt is calculated based on the liquid redistribution described in Section 2.5. Given the $\Delta V_{w,ij}$, the salt mole fraction after redistribution is determined by mass conservation using an implicit upwind scheme:

$$\begin{aligned} &x_{w,i}^{\mathrm{salt},\Gamma_b}\rho_{\mathrm{mol},w,i}^{\Gamma_b} V_i S_{w,i}^{\Gamma_b} + \sum_{m\to i} |\Delta V_{mi}| x_{\mathrm{w},m}^{\mathrm{salt},\Gamma_f}\rho_{\mathrm{mol},w,m}^{\Gamma_f} \\ &-\sum_{i\to k} |\Delta V_{ik}| x_{w,i}^{\mathrm{salt},\Gamma_f}\rho_{\mathrm{mol},w,i}^{\Gamma_f} = x_{w,i}^{\mathrm{salt},\Gamma_f}\rho_{\mathrm{mol},w,i}^{\Gamma_f} V_i S_{w,i}^{\Gamma_f}, \end{aligned} \tag{21}$$

where $x_{w,i}^{\mathrm{salt},\Gamma_b}$ and $x_{\mathrm{w},i}^{\mathrm{salt},\Gamma_f}$ are the salt mole fractions at pore i before and after redistribution, respectively, and $\rho_{\mathrm{mol},w,i}^{\Gamma_b}$ and $\rho_{\mathrm{mol},w,i}^{\Gamma_f}$ are the corresponding molar densities of liquid phase. $\sum_{m\to i}|\Delta V_{mi}| x_{w,m}^{\mathrm{salt},\Gamma_f}\rho_{\mathrm{mol},w,m}^{\Gamma_f}$ represents the total inflow of salt from neighboring pores m, and $\sum_{i\to k}|\Delta V_{ik}| x_{w,i}^{\mathrm{salt},\Gamma_f}\rho_{\mathrm{mol},w,i}^{\Gamma_f}$ represents the total outflow of salt from pore i to neighboring pores k.

To solve Equation 21, we introduce the auxiliary variable $c_i = x_{w,i}^{\mathrm{salt}}\rho_{\mathrm{mol},w,i}$ (i.e., the molar concentration of salt). Rearranging Equation 21 by collecting all unknown concentrations $\left(c_i^{\Gamma_f}\right)$ on the left-hand side yields the linear system for salt mass conservation:

$$\left(V_i S_{w,i}^{\Gamma_f} + \sum_{i\to k} |\Delta V_{ik}|\right) c_i^{\Gamma_f} - \sum_{m\to i} |\Delta V_{mi}| c_m^{\Gamma_f} = c_i^{\Gamma_b} V_i S_{w,i}^{\Gamma_b}. \tag{22}$$

This can be written in matrix form as $\mathbf{Ac} = \mathbf{b}$. The diagonal entries are $A_{ii} = V_i S_{w,i}^{\Gamma_f} + \sum_{i\to k} |\Delta V_{ik}|$, the off-diagonal entries are $A_{im} = -|\Delta V_{mi}|$ (for $m \neq i$), the vector of unknowns is $\mathbf{c} = \left\{c_1^{\Gamma_f}, c_2^{\Gamma_f}, \ldots, c_N^{\Gamma_f}\right\}^T$, and the right-hand side vector is $\mathbf{b} = \{b_1, b_2, \ldots, b_N\}^T$, with each component $b_i = c_i^{\Gamma_b} V_i S_{w,i}^{\Gamma_b}$. This linear system can then be solved directly to obtain the molar concentration $c_i^{\Gamma_f}$.

2.6.2. Diffusion of Dissolved Salt

The diffusion flux of dissolved salt between neighboring pores i and j is given by Fick's law:

$$J_{\text{diff},ij}^{\text{salt}} = -D_w^{\text{salt}} \frac{x_{w,i}^{\text{salt}} \rho_{\text{mol},w,i} - x_{w,j}^{\text{salt}} \rho_{\text{mol},w,j}}{l_{ij}}, \tag{23}$$

where D_w^{salt} is the diffusion coefficient of salt in the liquid phase, $x_{w,i}^{\text{salt}}$ and $x_{w,j}^{\text{salt}}$ are the salt mole fractions at the neighboring pores i and j, respectively, $\rho_{\text{mol},w,i}$ and $\rho_{\text{mol},w,j}$ are the corresponding molar densities of liquid phase, and l_{ij} is the length of pore throat ij. We advance the dissolved-salt concentrations with a backward Euler (fully implicit) discretization of the pore-wise mass balance:

$$\frac{x_{w,i}^{\text{salt},t_{n+1}} \rho_{\text{mol},w,i}^{t_{n+1}} - x_{w,i}^{\text{salt},t_n} \rho_{\text{mol},w,i}^{t_n}}{\Delta t} = \frac{1}{V_{w,i}^{t_{n+1}}} \sum_{j\in\mathcal{N}(i)} J_{\text{diff},ij}^{\text{salt},t_{n+1}} A_{w,ij}^{t_{n+1}}, \tag{24}$$

where Δt is the time step, $V_{w,i}^{t_{n+1}}$ is the liquid volume at pore i at time t_{n+1}, and $A_{w,ij}^{t_{n+1}}$ is the liquid phase cross-sectional area for diffusion in pore throat ij, which is determined by the invasion state of the pore throat ij and the liquid saturation of the pores i and j, as shown in Equation 38.

Similarly, we introduce the auxiliary variable c_i for the numerical solution. Rearranging Equation 24 and substituting Equation 23, we obtain:

$$c_i^{t_{n+1}} \left(1 + \frac{\Delta t}{V_{w,i}^{t_{n+1}}} \sum_{j\in\mathcal{N}(i)} D_w^{\text{salt}} \frac{A_{w,ij}^{t_{n+1}}}{l_{ij}}\right) - \sum_{j\in\mathcal{N}(i)} \left(\frac{\Delta t D_w^{\text{salt}} A_{w,ij}^{t_{n+1}}}{V_{w,i}^{t_{n+1}} l_{ij}}\right) c_j^{t_{n+1}} = c_i^{t_n}. \tag{25}$$

This can be written in the matrix form $\mathbf{A}\mathbf{c}^{t_{n+1}} = \mathbf{c}^{t_n}$, where $\mathbf{c}^{t_{n+1}}$ is the vector of unknown molar concentrations. This backward Euler discretization, which is unconditionally stable for pure diffusion, results in a large, sparse linear system i.e. solved efficiently using a sparse linear solver.

After solving for the molar concentration c_i from the advection and diffusion calculations, the mole fraction $x_{w,i}^{\text{salt}}$ is computed iteratively using $x_{w,i}^{\text{salt}} = c_i / \rho_{\text{mol},w,i}$, where $\rho_{\text{mol},w,i}$ is a function of $x_{w,i}^{\text{salt}}$ and can be evaluated using an equation of state for the brine solution.

2.7. Modeling of Salt Precipitation and Pore Space Alteration

2.7.1. Salt Precipitation

After the salt concentration is updated at the end of each time step or after each invasion event, we check for salt precipitation or dissolution based on the solubility limit, $x_{w,\,\text{max}}^{\text{salt}}$. We assume the reaction kinetics are instantaneous (i.e., local chemical equilibrium), meaning any salt concentration exceeding the solubility limit precipitates within the time step Δt (Bringedal et al., 2022). The volumetric source/sink term s_i^{salt} is therefore calculated as:

$$s_i^{\text{salt}} = \rho_{\text{mol},w}^{\max} \frac{\left(x_{w,i}^{\text{salt}} - x_{w,\max}^{\text{salt}}\right)}{\Delta t}, \tag{26}$$

where $\rho_{\text{mol},w}^{\max}$ is the molar density of the liquid phase at the solubility limit $x_{w,\max}^{\text{salt}}$.

2.7.2. Pore Space Alteration

Pore space alteration involves changes to the volume of both pore bodies and pore throats due to salt precipitation or dissolution. For a given pore body i, the volume fraction of the precipitated salt, $\phi_{s,i}$, is determined by the following equation:

$$\phi_{s,i} = \frac{V_{\text{salt},i}}{V_{\text{ini},i}}, \tag{27}$$

where $V_{\text{salt},i}$ is the volume of precipitated salt, $V_{\text{ini},i}$ is the initial volume of the pore body i. The change of $\phi_{s,i}$ during each time step is determined as follows:

$$\Delta\phi_{s,i} = \frac{\Delta V_{\text{salt},i}}{V_{\text{ini},i}} = \frac{s_i^{\text{salt}} V_{w,i} \Delta t}{\rho_{\text{mol},s} V_{\text{ini},i}}, \tag{28}$$

where $\rho_{\text{mol},s}$ is the molar density of the precipitated salt. The available volume of pore body i is updated as:

$$V_i^{t_{n+1}} = V_i^{t_n} - V_{\text{ini},i} \Delta\phi_{s,i}. \tag{29}$$

We assume the precipitated salt is distributed uniformly on the surface of the pore body. Based on this assumption, the radius of the pore body i after the precipitation/dissolution is updated as:

$$r_i^{t_{n+1}} = \left(\frac{V_i^{t_{n+1}}}{8}\right)^{1/3}. \tag{30}$$

For the pore throat, we assume it is volumeless, and we do not explicitly solve for precipitated salt within the throat. However, precipitated salt will still decrease its cross-sectional area, which in turn influences the hydraulic conductance. To account for this effect, we approximate the volume of precipitated salt in the pore throat, $\Delta V_{ij}^{t_n}$, using the precipitation source terms from the adjacent pore bodies (Schollenberger et al., 2024, 2025) at the current time step t_n:

$$\Delta V_{ij}^{t_n} = \frac{1}{2}\left(\frac{s_i^{\text{salt},t_n}}{A_i^{t_n}} + \frac{s_j^{\text{salt},t_n}}{A_j^{t_n}}\right) \frac{A_{ij}^{t_n} \Delta t}{\rho_{\text{mol},s}}, \tag{31}$$

where $A_i^{t_n}$ and $A_j^{t_n}$ are the cross-sectional areas of the adjacent pore bodies i and j at time t_n, respectively, and $A_{ij}^{t_n}$ is the cross-sectional area of the pore throat ij at time t_n. The radius of the pore throat ij for the next time step t_{n+1} is then updated as:

$$r_{ij}^{t_{n+1}} = \frac{1}{2}\left(\frac{V_{ij}^{t_n} - \Delta V_{ij}^{t_n}}{l_{ij}}\right)^{1/2}. \tag{32}$$

2.8. Local Rules for Pore Body and Pore Throat

2.8.1. Capillary Pressure-Saturation Relationship

The capillary pressure and saturation relationship is evaluated at the pore bodies. For the cubic pore body, the relationship is given as follows (Joekar-Niasar et al., 2010):

$$p_{c,i}(S_{w,i}, r_i) = \frac{2\sigma}{r_i(1 - \exp(-6.83S_{w,i}))}, \tag{33}$$

The inverse relation for $S_{w,i}$ follows as

$$S_{w,i}(p_{c,i}, r_i) = -\frac{1}{6.83} \ln\left(1 - \frac{2\sigma}{r_i p_{c,i}}\right). \tag{34}$$

2.8.2. Entry Pressure for Pore Throat

The entry pressure of a pore throat, p_{ij}^{entry}, is a critical parameter that determines the invasion event. This pressure represents the minimum capillary pressure required for the gas phase to displace the liquid and enter the throat. For a throat with a square cross-section, the entry pressure can be approximated as:

$$p_{c,ij}^{\text{entry}} = \frac{\sigma}{r_{ij}}\left[\cos\theta + \frac{1}{2}\sqrt{\pi - 3\theta + 3\sin\theta\cos\theta}\right], \tag{35}$$

where θ is the contact angle, which is assumed to be constant throughout the pore network.

2.8.3. Conductance for Pore Throat

The conductance model for a pore throat differs depending on whether it contains a single phase or two phases. When the throat is not invaded by the gas phase, it only provides conductance for the liquid. When the pore throat connects two pore bodies that are fully occupied by the gas phase, it only provides conductance for the gas. The conductance for single fluid phase flow in a square cross-section pore throat is given as (Patzek & Silin, 2001):

$$g_{\alpha,ij} = \frac{0.5623A_{ij}^2 G}{\mu_\alpha l_{ij}}, \tag{36}$$

where G is the shape factor, which is $1/16$ for the square cross-section, and μ_α is the viscosity of the fluid phase α.

For two-phase flow, since the liquid is the wetting phase, it will recede to the pore throat's corners while the gas phase occupies the central bulk void space. The conductance for the liquid phase (flowing in the corners) is given by (Ransohoff & Radke, 1988):

$$g_{w,ij} = \frac{r_{\text{am}}^2}{\mu_w l_{ij}} \sum_{\Lambda=1}^{n_{\text{corner}}} \frac{A_{w,\Lambda}}{\xi_\Lambda}, \tag{37}$$

where $r_{\text{am}} = \sigma/\max\{p_{c,i}, p_{c,j}\}$ is the radius of curvature of the arc menisci, n_{corner} is the number of corners in the pore throat (e.g., 4 for a square), and ξ_Λ is a dimensionless resistance factor, for which we use the method proposed by Zhou et al. (1997). $A_{w,\Lambda}$ is the area of the liquid in corner Λ, calculated as follows:

$$A_{w,\Lambda} = r_{\text{am}}^2\left[\frac{\cos\theta\cos(\theta + \alpha_h)}{\sin\alpha_h} + \alpha_h + \theta - \frac{\pi}{2}\right], \tag{38}$$

where α_h is the half angle of the corner Λ, which is $\pi/4$ for the square cross-section.

To account for the potential loss of hydraulic connectivity at low liquid saturation, we introduce a threshold capillary pressure $p_{c,i}^{\text{thr}}$ for each pore body, above which the corner liquid in pore body i becomes hydraulically disconnected from its neighbors (S. Chen et al., 2020). Following Wan and Tokunaga (1997), this threshold is given by

$$p_{c,i}^{\text{thr}} = \frac{9.068\,\sigma}{2\,r_i}. \tag{39}$$

Accordingly, the liquid conductance of pore throat ij is modified as

$$\tilde{g}_{w,ij} = \delta_{ij}\, g_{w,ij}, \qquad \delta_{ij} = \begin{cases} 0, & p_{c,i} > p_{c,i}^{\mathrm{thr}} \text{ or } p_{c,j} > p_{c,j}^{\mathrm{thr}}, \\ 1, & \text{otherwise}, \end{cases} \tag{40}$$

where δ_{ij} is a Boolean indicator that removes the corner-liquid conductance of pore throat ij whenever either of the two adjacent pore bodies has exceeded its disconnection threshold. As a consequence, an originally connected invaded cluster may split into multiple hydraulically independent sub-clusters during drying.

The conductance for the gas phase is given by (Bakke & Øren, 1997):

$$g_{g,ij} = \frac{r_{\mathrm{eff}}^2 A_{g,ij}}{8\mu_g l_{ij}}, \tag{41}$$

where μ_g is the gas viscosity, $A_{g,ij}$ is the cross-sectional area occupied by the gas phase, given by $A_{g,ij} = A_{ij} - \sum A_{w,\Lambda}$, and r_{eff} is the effective radius, calculated as:

$$r_{\mathrm{eff}} = \frac{1}{2}\left(\sqrt{\frac{A_{g,ij}}{\pi}} + r_{ij}\right). \tag{42}$$

2.9. Computational Algorithms

Given the above formulations, the computational workflow of the proposed QSPNM framework is outlined as follows and illustrated in Figure 4:

(i) Initialization: Initialize the pore-network model with the given structure and initial conditions. Define the top pore bodies as the evaporative surface, which provides the driving force for the drying process.
(ii) Vapor Diffusion: Starting from the state at t_n, solve the vapor diffusion in the gas phase over the time interval $[t_n, t_{n+1}]$. Use the resulting phase-change fluxes to update the liquid mass and salt concentration in each pore body.
(iii) Drying-induced Liquid Redistribution: Based on the updated liquid saturation from step (ii), solve the capillary equilibrium within each invaded cluster to redistribute the liquid phase.
(iv) Salt Advection: Compute the time-integrated liquid volume transfer resulting from the drying-induced redistribution in step (iii), and solve the advective salt transport to update the salt concentration in each pore body.
(v) Salt Diffusion: Starting from the state at t_n, solve the salt diffusion in the liquid phase over the time interval $[t_n, t_{n+1}]$ and update the salt concentration and liquid saturation in each pore body.
(vi) Invasion Check: Based on the predicted capillary state after steps (ii)–(v), check whether an invasion event is triggered within $[t_n, t_{n+1}]$. If an invasion is detected, locate the earliest invasion time $t_{\mathrm{inv}} \in (t_n, t_{n+1}]$, restore the backed-up state at t_n, and recompute steps (ii)–(v) over the reduced interval $[t_n, t_{\mathrm{inv}}]$ with $\Delta t_\star = t_{\mathrm{inv}} - t_n$. Then execute the invasion, update the invaded cluster, solve the invasion-induced capillary redistribution, and compute the corresponding advective salt transport from the resulting time-integrated liquid flux $\Delta V_{\mathrm{w},ij}$. If no invasion is detected, proceed directly to step (vii).
(vii) Salt Precipitation: Apply salt precipitation/dissolution and update the pore-body volume and throat radius using the actual advanced time interval. This interval is Δt when no invasion occurs and $\Delta t_\star = t_{\mathrm{inv}} - t_n$ when an invasion occurs.

If no invasion is detected, the global time advances from t_n to t_{n+1}. If an invasion occurs within the current time step, the algorithm advances only to t_{inv}, performs the invasion-induced update, applies precipitation and updates the geometry using $\Delta t_\star$, and then continues from the updated state at t_{inv}.

The simulation proceeds iteratively by returning to step (ii) with the updated pore network geometry. This approach effectively discretizes the continuous dynamic process of evaporation-driven salt precipitation into a sequence of quasi-static equilibrium states, advancing until the target simulation time is reached. All algorithms

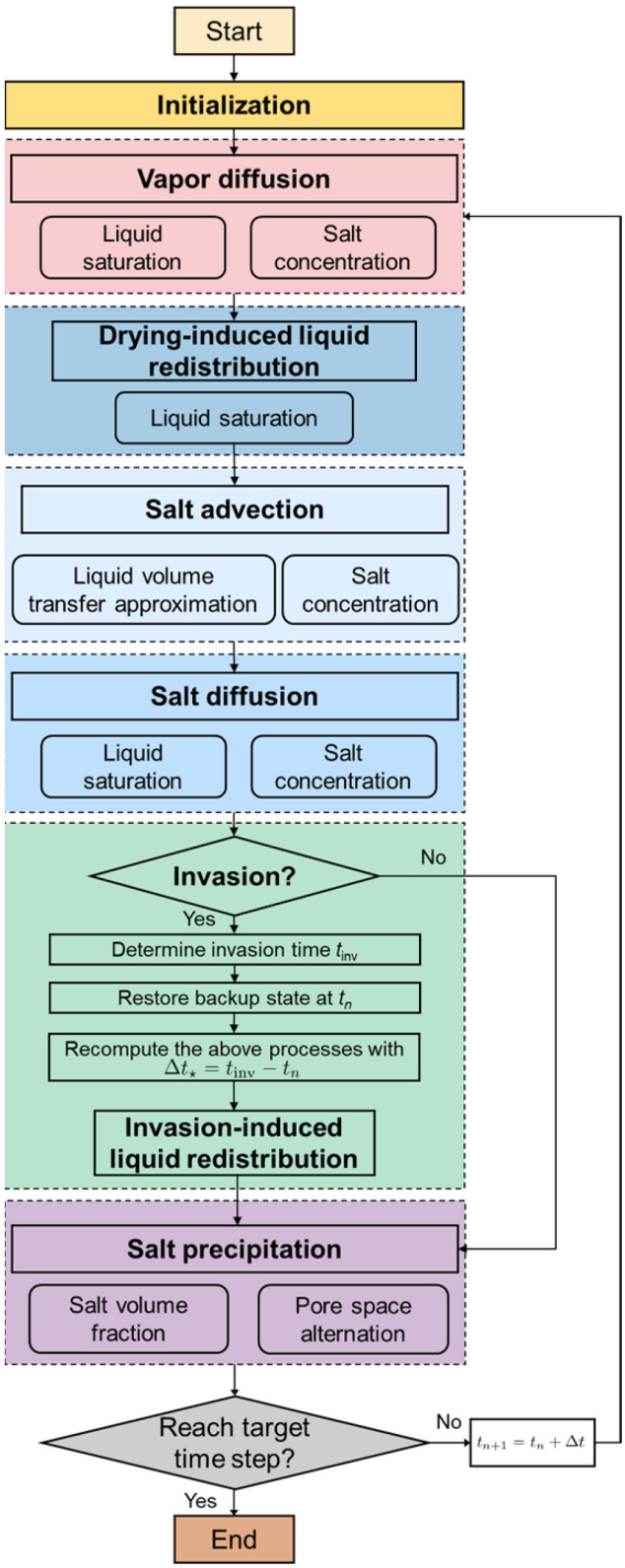

Figure 4. Diagram of overall numerical implementation for simulation of evaporation-driven salt transport and precipitation.

and procedures detailed herein were implemented using our self-developed Python source code. The detailed pseudocode is provided as Algorithm S1 in the Supporting Information S1.

3. Numerical Experiments

We apply the proposed QSPNM framework to simulate the evaporation-driven salt transport and precipitation processes in porous media, considering both pure water evaporation and brine evaporation. We choose sodium chloride (NaCl) as the representative salt for this simulation. The proposed QSPNM is compared against a DPNM (Schollenberger et al., 2025) under identical simulation conditions. Furthermore, a large pore network is employed to demonstrate the computational capacity of the proposed framework. Since the primary objective of this section is to verify the proposed QSPNM against the established DPNM, the benchmark cases employ small pore networks (PN1–PN3) so that the computationally expensive DPNM remains feasible and a detailed, pore-by-pore comparison can be performed. These benchmark networks are deliberately chosen with increasing dimensionality and heterogeneity to systematically test different aspects of the model formulation. Below, we present details of the pore network structures, initial and boundary conditions, and a comparative analysis of key quantities between the two models.

3.1. Pore Network Structures

We use three different pore network structures (PN1, PN2, and PN3) for the benchmark cases and one large pore network structure (PN4) for the showcase, as illustrated in Figure 5. PN1 is a 1D pore network with 6 homogeneous pore bodies and their connecting pore throats; PN2 is a 2D network consisting of 5×6 pore bodies (pore body radius standard deviation σ_r is 10 μm); PN3 is a 3D network consisting of $2 \times 2 \times 3$ pore bodies ($\sigma_r = 20$ μm); and PN4 is a large 3D network consisting of $30 \times 30 \times 60$ pore bodies ($\sigma_r = 20$ μm). For all networks, the average pore body radius is 270 μm, the distance between pore bodies is 700 μm, and the pore bodies are connected by pore throats with square cross-sections. The pore bodies at the top are defined as the evaporative surface. To better represent this evaporation boundary condition, the pore throats laterally connecting these top pore bodies are removed, which is consistent with previous studies (Schollenberger et al., 2025; Weishaupt et al., 2022). For the benchmark cases (PN1–PN3), the QSPNM and the DPNM are run on exactly the same network realization, making the comparison deterministic. Ensemble averaging over multiple random realizations is therefore not required for the purpose of model verification. Nevertheless, when the QSPNM is applied to study macroscopic transport behavior in disordered media, statistical averaging over multiple realizations would be necessary, and the computational efficiency of the QSPNM makes such ensemble studies feasible.

3.2. Initial and Boundary Conditions

For each pore network structure, we perform simulations of both pure water and brine evaporation. The porous medium is exposed at the top to a stagnant atmosphere ($p = 100$ kPa, $T = 293.15$ K) containing unsaturated water vapor ($x^w_{g,\mathrm{amb}} = 4.7 \times 10^{-3}$), while all other boundaries are impermeable. A Neumann boundary condition is applied at the top surface following

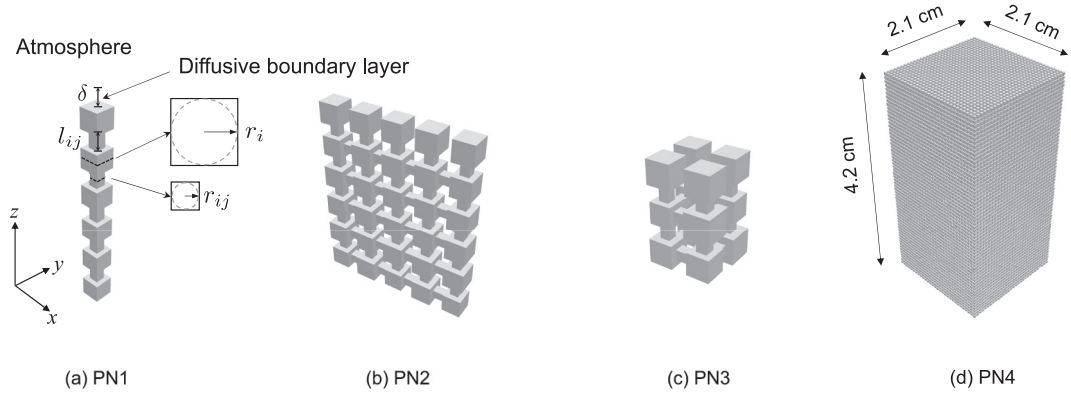

Figure 5. Pore network structures for the benchmark cases (PN1, PN2, and PN3) and showcase (PN4). Note: Dimensions are not to scale.

Equation 2, assuming a constant diffusive boundary layer thickness of $\delta = 1600$ μm. This value is selected based on the range suggested by Shahraeeni et al. (2012). Zero-flux conditions are applied at all other boundaries. Under these conditions, Ca for all simulations remains below 3×10^{-9}, which confirms that the drying process falls within the capillary-dominated regime.

Initially, the pore network is highly saturated, with a liquid saturation of $S_w = 0.9$. The initial salt mole fraction, x_w^{NaCl}, is set to 0 for the pure water evaporation cases (Cases 1–4) and 0.08 for the brine evaporation cases (Cases 5–8). The initial salt concentration is assumed to be uniform throughout the entire pore network. A summary of the geometric parameters, initial conditions, and boundary conditions for these simulation cases is provided in Table 1.

3.3. Comparative Analysis of Key Quantities

We evaluate the performance of our proposed QSPNM by comparing its results against those of a DPNM. The comparison focuses on key physical quantities: for pure water evaporation, we analyze the liquid saturation (S_w)

Table 1
Parameters of Simulation Cases for Evaporation-Driven Salt Precipitation

	Pure water evaporation				Brine evaporation			
	Case 1	Case 2	Case 3	Case 4	Case 5	Case 6	Case 7	Case 8
Geometry								
Structure	PN1	PN2	PN3	PN4	PN1	PN2	PN3	PN4
Mean r_i (μm)	270	270	270	270	270	270	270	270
σ_r (μm)	0	10	20	20	0	10	20	20
Initial conditions								
$x_{\mathrm{w}}^{\mathrm{NaCl}}$ (−)	0	0	0	0	0.08	0.08	0.08	0.08
S_{w} (−)	0.9							
p_{g} (kPa)	100							
ϕ_s (−)	0							
Boundary conditions								
$x_{\mathrm{g,amb}}^{\mathrm{w}}$ (−)	4.7×10^{-3}							
$p_{\mathrm{g,amb}}$ (kPa)	100							
δ (μm)	1600							

distribution; for brine evaporation, the analysis is extended to include salt concentration $\left(x_w^{\mathrm{NaCl}}\right)$ and precipitated salt $\left(\phi_s\right)$ distributions.

The discrepancy between the models is quantified using a volume-weighted, spatio-temporal absolute L^2 error. This absolute error, $E_u(y)$, is calculated over the set of all pore bodies $\mathcal{N}$ and all time steps n for a given quantity $y \in \left\{S_w, x_w^{\mathrm{NaCl}}, \phi_s\right\}$:

$$E_u(y) = \sqrt{\frac{\sum_n \sum_{i \in \mathcal{N}} V_{\mathrm{ini},i} \left(\hat{y}_i^{t_n} - y_i^{t_n}\right)^2}{\sum_n \sum_{i \in \mathcal{N}} V_{\mathrm{ini},i}}} \tag{43}$$

where $\hat{y}_i^{t_n}$ is the value from the QSPNM (our model) and $y_i^{t_n}$ is the reference value from the DPNM in pore i at time t_n. Note that $E_u(y)$ represents an absolute error, quantifying the magnitude of the difference between the two models.

Additionally, we assess the numerical convergence of both the QSPNM and the DPNM by running simulations with four different time step sizes: $\Delta t = 0.01$ s, $\Delta t = 0.1$ s, $\Delta t = 0.5$ s, and $\Delta t = 1$ s. To evaluate this convergence, we reuse the absolute L^2 error formula (Equation 43), but the variables are redefined. In this context, $y_i^{t_n}$ (the reference) is the solution obtained with the smallest time step ($\Delta t = 0.01$ s), and $\hat{y}_i^{t_n}$ represents the results from the simulations with coarser time steps ($\Delta t = 0.1$ s, 0.5 s, and 1 s). The resulting absolute errors relative to this reference solution are denoted as $E_u(y)_{\Delta t = 0.1\mathrm{s}}$, $E_u(y)_{\Delta t = 0.5\mathrm{s}}$, and $E_u(y)_{\Delta t = 1\mathrm{s}}$, respectively.

4. Results and Analysis

Based on the simulation setup mentioned above, we conduct a series of simulations to evaluate the validity, numerical convergence, and computational efficiency of the proposed QSPNM against the DPNM. Furthermore, to demonstrate the model's computational capability, we present an application of the proposed QSPNM on a large pore network. These results are detailed and discussed in the following sections.

4.1. Comparison of the QSPNM With the DPNM

Here, we compare the proposed QSPNM against the DPNM for both pure water and brine evaporation scenarios, using a time step of $\Delta t = 0.01$ s. The absolute L^2 error, $E_u(y)$, for selected quantities is calculated according to the method described in Section 3.3.

4.1.1. Pure Water Evaporation Scenario

4.1.1.1. Comparison of Liquid Saturation Distribution

Figure 6 shows the liquid saturation distributions during pure water evaporation from both the QSPNM and the DPNM for the three different pore network structures (Cases 1–3). Visually, the results from both models are in good agreement for all three cases. In Case 1 (the homogeneous 1D network), evaporation causes the throats to be invaded sequentially from top to bottom. When a throat is invaded, the adjacent uninvaded pore body is subsequently invaded by the gas phase. The liquid previously stored in this pore body is then redistributed to the invaded cluster, driven by the capillary pressure difference via corner flow. For Case 2 (the heterogeneous 2D network), the QSPNM also captures the drying pattern well, showing results consistent with the DPNM. Furthermore, the QSPNM performs well for Case 3 (the heterogeneous 3D network), which has a larger coordination number. To quantitatively assess the accuracy, we calculated the absolute L^2 error $E_u(S_w)$ for the liquid saturation distributions in all three cases. As shown in Figure 7, the calculated absolute L^2 error $E_u(S_w)$ for all three cases is less than 0.02. This indicates that our proposed QSPNM is in good agreement with the DPNM for simulating pure water evaporation in porous media. This result provides a solid foundation for the subsequent simulation of brine evaporation.

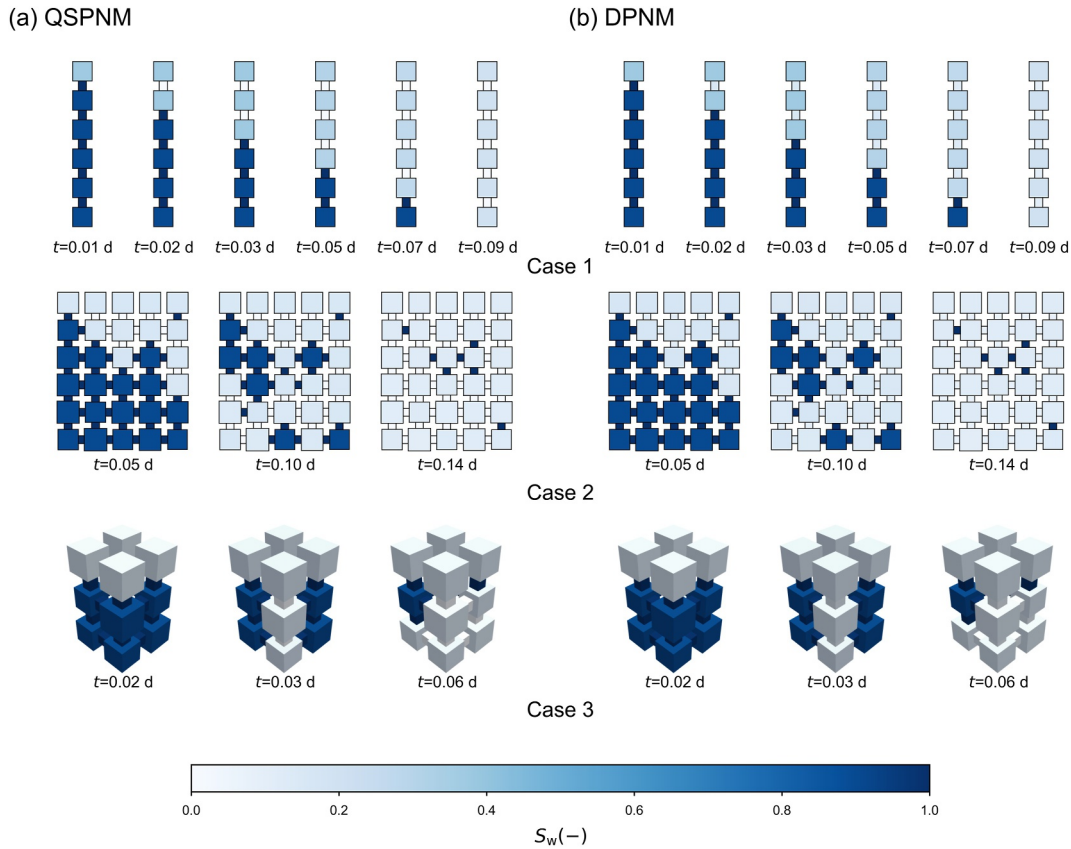

Figure 6. Comparison of liquid saturation distribution during pure water evaporation with $\Delta t = 0.01$ s: (a) QSPNM and (b) DPNM.

4.1.1.2. Comparison of Time-Integrated Liquid Flux Approximation With Different $g_{w,ij}$

As mentioned in Section 2.5, it is essential to approximate the $\Delta V_{w,ij}$ during both end-of-time-step and invasion event redistributions to compute advective salt transport. To evaluate the approximation proposed in this study, we compare it against the DPNM, from which the reference solution for $\Delta V_{w,ij}$ is obtained. Although the redistribution process is mechanistically similar for both drying steps and invasion events, the magnitude of the

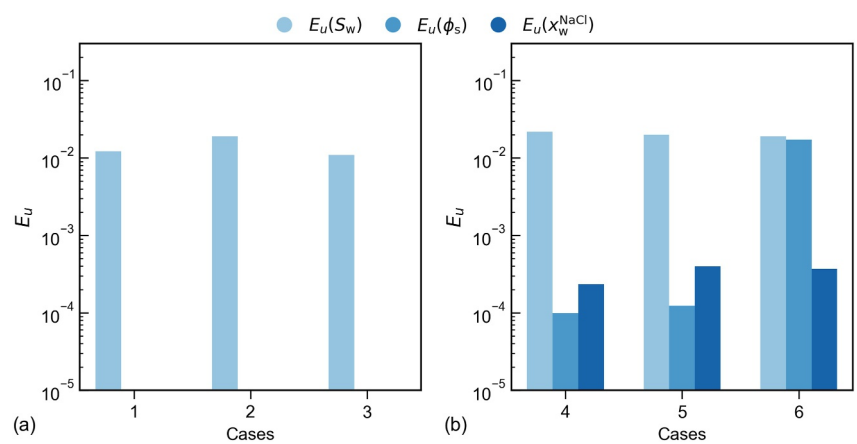

Figure 7. Absolute L^2 error between the QSPNM and the DPNM with $\Delta t = 0.01$ s during (a) pure water evaporation (Cases 1–3) and (b) brine evaporation (Cases 5–7).

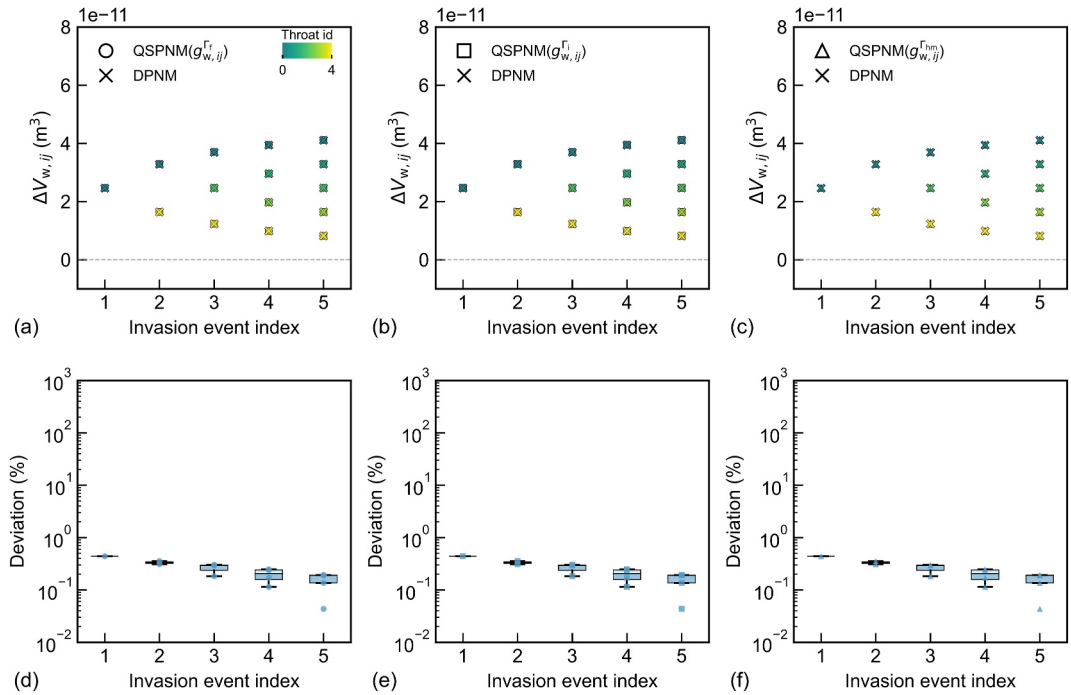

Figure 8. Comparison of $\Delta V_{w,ij}$ between the QSPNM and the DPNM in PN1. (a–c) Scatter plots of $\Delta V_{w,ij}$ from the QSPNM (using $g^{\Gamma_i}_{w,ij}$, $g^{\Gamma_f}_{w,ij}$, and $g^{\Gamma_{hm}}_{w,ij}$) versus the DPNM reference. (d–f) Corresponding relative deviations for the three conductance models.

redistributed volume is much more significant during an invasion (see Figures 3a4 and 3b4). Therefore, we focus on the $\Delta V_{w,ij}$ during invasion events as a representative case for validating our QSPNM approximation.

In the DPNM, the liquid volume flux in the throats varies significantly once the gas phase invades a throat connecting to a previously uninvaded pore body. The liquid volume transfer during this invasion event is therefore obtained by integrating the liquid volume flux over this variation period. As this time interval is short, the simulation time step is refined to 0.001 s to achieve more accurate results.

In the QSPNM, we employ the approximation method proposed in Section 2.5. A critical parameter in this approximation is the conductance of the newly invaded throat, as its value decreases significantly during the invasion. The choice of this conductance, $g^{\Gamma_*}_{w,ij}$, therefore strongly influences the result. Here, we compare three different models for this conductance, as mentioned in Section 2.5: the conductance before invasion $\left(g^{\Gamma_i}_{w,ij}\right)$, the conductance after invasion $\left(g^{\Gamma_f}_{w,ij}\right)$, and the harmonic mean of the two $\left(g^{\Gamma_{hm}}_{w,ij}\right)$. A positive value for $\Delta V_{w,ij}$ indicates that the net liquid flow during the invasion event is in the positive geometric coordinate direction (shown in Figure 5). The relative error of liquid transfer in each throat is calculated for comparison, defined as:

$$\epsilon_{\Delta V_{w,ij}} = \frac{\left|\Delta V^{\mathrm{QSPNM}}_{w,ij} - \Delta V^{\mathrm{DPNM}}_{w,ij}\right|}{\left|\Delta V^{\mathrm{DPNM}}_{w,ij}\right|} \times 100\% \tag{44}$$

where $\Delta V^{\mathrm{QSPNM}}_{w,ij}$ and $\Delta V^{\mathrm{DPNM}}_{w,ij}$ are the time-integrated liquid fluxes during the invasion event calculated by QSPNM and DPNM, respectively.

As shown in Figure 8, the time-integrated liquid flux calculated by the QSPNM (using all three conductance models) is in good agreement with the DPNM results for the 1D case, with the median relative error below 1%. The relative errors for the three conductance models are identical in all 1D invasion events. This is because in the 1D case, the liquid flow direction is fixed along the single path connecting the pore bodies. The throat

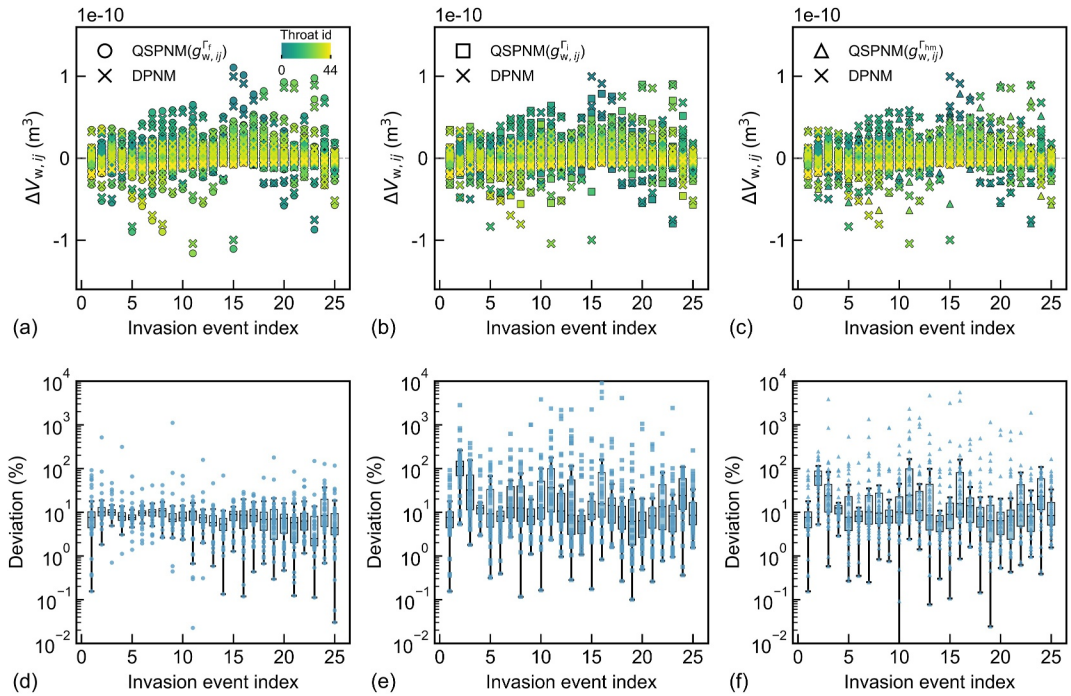

Figure 9. Comparison of time-integrated liquid flux ($\Delta V_{w,ij}$) between the QSPNM and the DPNM in PN2. (a–c) Scatter plots of $\Delta V_{w,ij}$ from the QSPNM (using $g^{\Gamma_i}_{w,ij}$, $g^{\Gamma_f}_{w,ij}$, and $g^{\Gamma_{hm}}_{w,ij}$) versus the DPNM reference. (d–f) Corresponding relative deviations for the three conductance models.

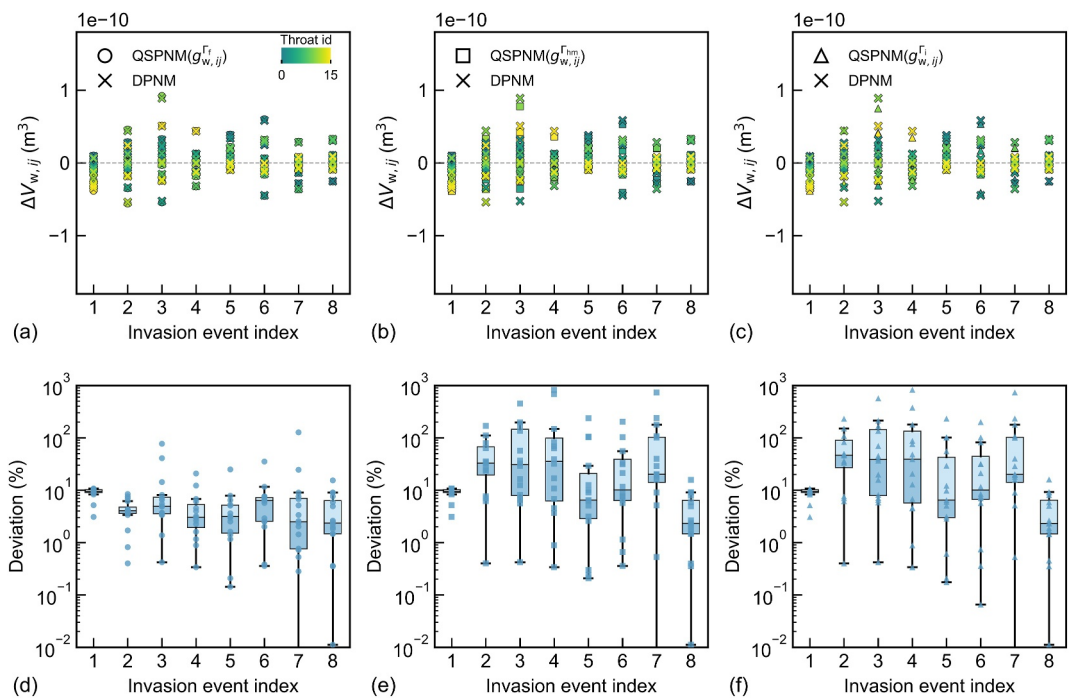

Figure 10. Comparison of time-integrated liquid flux ($\Delta V_{w,ij}$) between the QSPNM and the DPNM in PN3. (a–c) Scatter plots of $\Delta V_{w,ij}$ from the QSPNM (using $g^{\Gamma_i}_{w,ij}$, $g^{\Gamma_f}_{w,ij}$, and $g^{\Gamma_{hm}}_{w,ij}$) versus the DPNM reference. (d–f) Corresponding relative deviations for the three conductance models.

conductance, which represents flow resistance, affects the duration of the flow but not the total volume of liquid transferred, as the final equilibrium state is predetermined.

In contrast, the 2D and 3D pore network structures (Figures 9 and 10) show that the relative errors for the three models diverge significantly. Among these, the model using the throat conductance after invasion $\left(g_{w,ij}^{\Gamma_f}\right)$ yields the smallest relative error, while the model using the conductance before invasion $\left(g_{w,ij}^{\Gamma_i}\right)$ performs the worst. This discrepancy arises because in 2D and 3D networks, the higher coordination number allows liquid to redistribute via multiple paths to reach the same final equilibrium. Under this condition, the resistance of each pore throat strongly dictates the partitioning of the liquid transfer among these different directions. As shown in Equation 36 and Equation 37, throat conductance decreases significantly upon invasion (transitioning from bulk to film flow), but changes negligibly with further saturation variations once it is invaded (Schneider et al., 2025). Therefore, the primary difference between the three models lies in how they treat the newly invaded throat.

In the DPNM, this dynamic process is resolved such that the newly invaded throat immediately adopts its low, post-invasion conductance. This DPNM behavior is best mimicked by the QSPNM model using $g_{w,ij}^{\Gamma_f}$, rather than $g_{w,ij}^{\Gamma_i}$ (the pre-invasion conductance) or the harmonic mean. This conclusion is confirmed by the comparison results illustrated in Figures 9 and 10. The median $\epsilon_{\Delta V_{w,ij}}$ for the best-performing model $\left(g_{w,ij}^{\Gamma_f}\right)$ is already below 10%. It should be noted that refining the DPNM time step (which increases the accuracy of the DPNM reference solution) would likely decrease this error value even further. Therefore, we use the QSPNM with $g_{w,ij}^{\Gamma_f}$ for the time-integrated liquid flux approximation and calculation of advective salt transport in the simulations for brine evaporation.

4.1.2. Brine Evaporation Scenario

Brine evaporation is simulated using the same pore network structures as the pure water scenarios, but with an initial x_w^{NaCl} of 0.08. The boundary conditions are identical to those used in the pure water cases, as shown in Table 1. Based on the calculation of $\Delta V_{w,ij}$ that is validated against the DPNM, the QSPNM framework sequentially solves for salt migration and precipitation. The comparisons of liquid saturation, salt concentration, and precipitated salt distributions for both the QSPNM and the DPNM are provided in Figures S1–S3 of Supporting Information S1. It can be seen that during brine evaporation, throats are invaded sequentially, similar to the pure water case. However, the overall water saturation evolves much more slowly than in the pure water process. This is due to the influence of salt concentration on the saturated vapor pressure, as described by Equation 3. During this process, salt is transported to the top of the pore network via capillary-driven flow. x_w^{NaCl} in the uninvaded pore bodies also increases due to diffusion. Once the salt concentration reaches the solubility limit, salt precipitates typically at the top pore bodies of the pore network. This precipitation reduces the available pore body volume and alters the local capillary pressure-saturation relationship, which further inhibits the evaporation process.

As illustrated in Figures S1–S3 of Supporting Information S1, the proposed QSPNM well reproduces the water saturation evolution, salt concentration evolution, and salt precipitation patterns of the DPNM when using the same pore network structures and boundary conditions. Furthermore, as depicted in Figure 7, the absolute L^2 errors ($E_u(S_w)$, $E_u\left(x_w^{\mathrm{NaCl}}\right)$, and $E_u(\phi_s)$) between the QSPNM and the DPNM (using $\Delta t = 0.01$ s) are all less than 0.02, which further verifies the accuracy of the proposed QSPNM framework. This indicates that the proposed framework can be adopted as a substitute for the DPNM within the studied regime where Ca is relatively small. In the following sections, we will further demonstrate the advantages of the proposed QSPNM framework in terms of numerical convergence and computational performance.

4.2. Comparison of Numerical Convergence

The temporal convergence of the key quantities during both pure water and brine evaporation is summarized in Figure 11. For the DPNM, the absolute L^2 error $E_u(y)$ in cases with PN1 and PN2 is relatively small when compared to the reference solution (at $\Delta t = 0.01$ s) and exhibits a clear convergence trend as the time step size decreases. This indicates that the DPNM achieves acceptable convergence for these networks even with larger time steps.

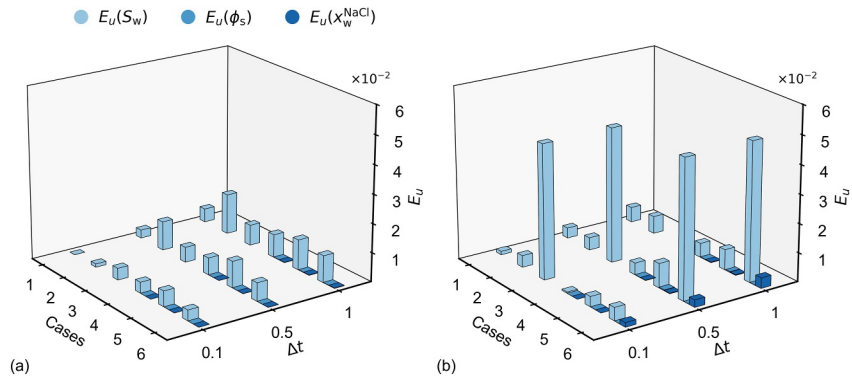

Figure 11. Temporal convergence of key quantities comparing different Δt against the reference ($\Delta t = 0.01$ s): (a) QSPNM and (b) DPNM.

However, for the cases with PN3, the $E_u(S_w)$ for the DPNM is relatively large (around 0.05) and fails to decrease significantly as the time step size is reduced. Furthermore, the DPNM simulation for Case 3 failed to converge with $\Delta t = 1$ s. To investigate the reason for this numerical instability, we compare snapshots of the liquid distribution in Case 3 for $\Delta t = 0.1$ s and $\Delta t = 0.01$ s (Figure 12). At $t = 5000$ s, the liquid distributions for both time steps are identical. An invasion event occurs between 5000 s and 5600 s, which reveals the source of the error: in the $\Delta t = 0.01$ s reference solution, only throat T2 is invaded, while in the $\Delta t = 0.1$ s simulation, throats T1 and T2 are erroneously invaded simultaneously. This fundamental divergence in the invasion path is the direct cause of the large error observed in the DPNM.

To understand the underlying cause of this divergence, we extracted the radii (r_{ij}) of these two throats, which control the invasion events. We found that r_{ij}(T1) = 127.42 μm and r_{ij}(T2) = 127.43 μm. These radii are extremely close, but distinct. This small difference is the direct cause of the error. The $\Delta t = 0.01$ s simulation has sufficient temporal resolution to differentiate this small deviation, correctly predicting the invasion of T2 first (which has the slightly larger radius and thus the lower entry pressure). However, the larger time step of $\Delta t = 0.1$ s is too coarse to resolve the small difference between these entry pressures, leading to an inaccurate simultaneous invasion.

In contrast, the proposed QSPNM achieves stable convergence for all cases, even with $\Delta t = 1$ s. As shown in Figure 11, the absolute L^2 errors $E_u(y)$ for all quantities across all 6 cases are below 0.02 and exhibit a clear convergence trend as Δt decreases. In the challenging PN3 cases, the QSPNM accurately predicts the invasion sequence, correctly distinguishing the throat radius difference between T1 and T2 even at large time steps. This numerical robustness stems from two key factors. Primarily, the QSPNM treats liquid redistribution as an instantaneous process that does not need to be resolved as a transient process, and it employs a physical criterion (Equation 12) that verifies whether the capillary pressure has crossed the minimum entry threshold during the time step, making it far less susceptible to failures when pore throats connecting to the invaded cluster have nearly

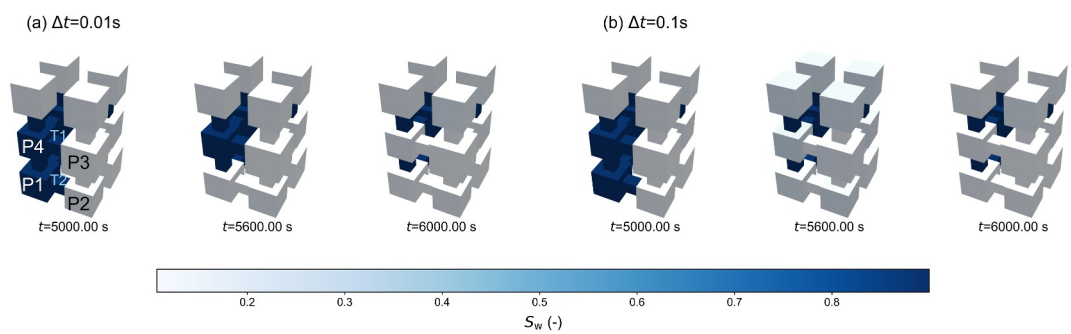

Figure 12. Comparison of liquid distribution in Case 3 with Δt of (a) 0.01 s and (b) 0.1 s.

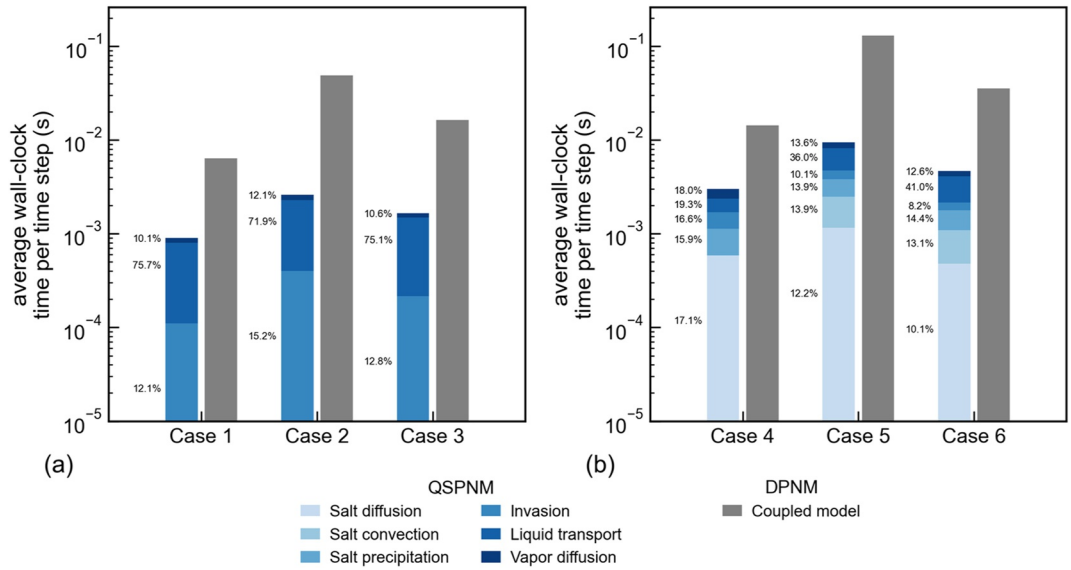

Figure 13. Comparison of computational performance between the QSPNM and the DPNM: (a) pure water evaporation scenario and (b) brine evaporation scenario.

equal radii. Secondly, the use of an implicit time scheme for salt transport ensures that this part of the calculation remains unconditionally stable, regardless of the time step size.

Therefore, the QSPNM's time-step constraint is far less restrictive. It is primarily determined by the accuracy of the subsequent invasion time interpolation (see Equations 13 and 14), rather than the DPNM's restrictive requirement to resolve the invasion dynamics themselves. This allows the proposed QSPNM to achieve acceptable simulation results with a significantly larger time step, thereby substantially improving computational performance.

4.3. Comparison of Computational Performance

As mentioned in Section 2, in the proposed QSPNM framework, the vapor diffusion, liquid redistribution, salt transport, and precipitation are decoupled and solved sequentially. It is expected that the computational time per time step for the QSPNM is less than that of the DPNM, as the DPNM solves the coupled system with a fully implicit scheme. To compare the computational performance of the two models, we use the average wall-clock time per time step as the primary metric. This metric is preferred over the total runtime of a complete simulation because the latter also depends on the total simulated physical time of each case. The average per-step cost therefore provides a more normalized measure of the intrinsic computational burden of each method. Since the DPNM requires much smaller time steps to converge when invasion events occur, this per-step comparison is conservative with respect to the practical total cost of reaching the same physical end time. To further investigate the computational performance of both models, the average wall-clock time per time step for all cases is extracted and compared in Figure 13. For the QSPNM, since we solve the processes sequentially, the computational time for each sub-process can also be analyzed separately.

Figure 13a shows the results for the pure water evaporation scenario. The average wall-clock time per time step increases for both QSPNM and DPNM as the pore network structure becomes more complex. Furthermore, the wall-clock time for the QSPNM is significantly lower than that of the DPNM. The QSPNM is approximately 6.9–18.6 times faster, which demonstrates the efficiency of the proposed framework. Additionally, the relative computational cost (as a percentage) for each QSPNM sub-process is similar among the three cases. The liquid redistribution step is the most time-consuming. It accounts for approximately 76%–78% of the total time per step. This high cost is due to the cluster-based capillary pressure equilibration (Equation 10). This step requires graph connectivity analysis and nonlinear equation solving for each connected cluster at every time step. Invasion prediction is the second most expensive step, consuming around 15% of the total time. Vapor diffusion is the least computationally demanding, as it only requires solving a linear system for mass conservation in the invaded

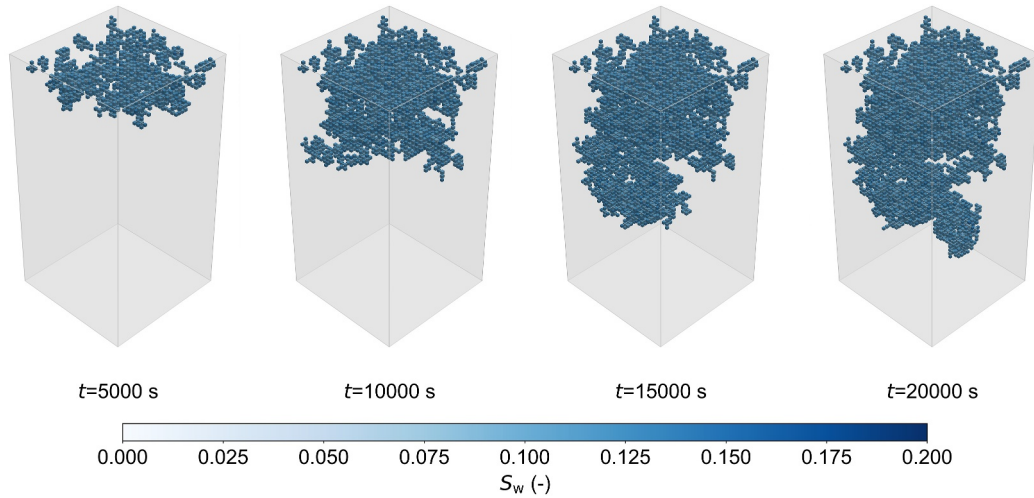

Figure 14. Liquid phase saturation evolution within the invaded cluster during pure water evaporation on PN4.

cluster (Equation 5). For the brine evaporation scenario, as illustrated in Figure 13b, the wall-clock time per time step for the QSPNM is still much less than that of the DPNM, at 5.5 to 13.6 times faster. This deviation increases with the complexity of the pore network structure, which demonstrates the efficiency of the proposed QSPNM framework in brine evaporation scenarios, especially for large pore network structures. For the DPNM, the wall-clock time per accepted time step increases by around 2.2 to 2.6 times compared to the pure water evaporation scenario. This is due to the increased computational cost of assembling the global matrix for the nonlinear governing equations. For the QSPNM, the added complexity of solving salt transport and precipitation increases the wall-clock time per time step by approximately 2.8–3.6 times compared to the pure water evaporation scenario. Liquid transport still consumes the most time, accounting for around 36%–43.5% of the total time per step. The solving of salt transport and precipitation combined accounts for around 34.5%–40% of the wall-clock time for each step.

4.4. Application of QSPNM on a Large 3D Pore Network

Building on its enhanced numerical convergence and computational efficiency, the proposed QSPNM is applied to a large 3D pore network structure (PN4, see Figure 5) for both pure water and brine evaporation, which are scenarios that are computationally very demanding for DPNMs. The simulations utilize a time step size of 1 s.

For PN4, the average wall-clock time per time step of the QSPNM is 2.45 s for pure water evaporation and 13.85 s for brine evaporation. For comparison, the DPNM is computationally very demanding for PN4 and only converges for sufficiently small time-step sizes. Its performance was therefore evaluated over the first 100 s of simulated physical time. Based on this interval, the average wall-clock time per accepted time step of the DPNM is approximately 127.95 s for pure water evaporation and 333.10 s for brine evaporation. This confirms that, for such large pore networks, the computational cost of the DPNM is drastically higher than that of the QSPNM, making the QSPNM the more practical choice for large-scale simulations. Figure 14 illustrates the liquid phase saturation evolution within the invaded cluster during pure water evaporation. For the brine case, the liquid phase saturation, salt concentration, and precipitated salt evolutions within the invaded cluster are depicted in Figure 15. These results demonstrate the capability of the proposed QSPNM to model larger pore networks close to a representative elementary volume, offering a promising tool for developing upscaling strategies and REV-scale descriptions of evaporation-driven salt transport and precipitation in porous media.

5. Conclusions

We have developed a new QSPNM framework for evaporation-driven salt transport and precipitation in porous media. The model captures the complex interplay of vapor diffusion, capillary-driven corner flow, invasion, salt diffusion, advection, and precipitation at the pore scale. To incorporate the contribution of corner flow to salt advection and precipitation, we have derived an approximation method to compute the time-integrated liquid flux

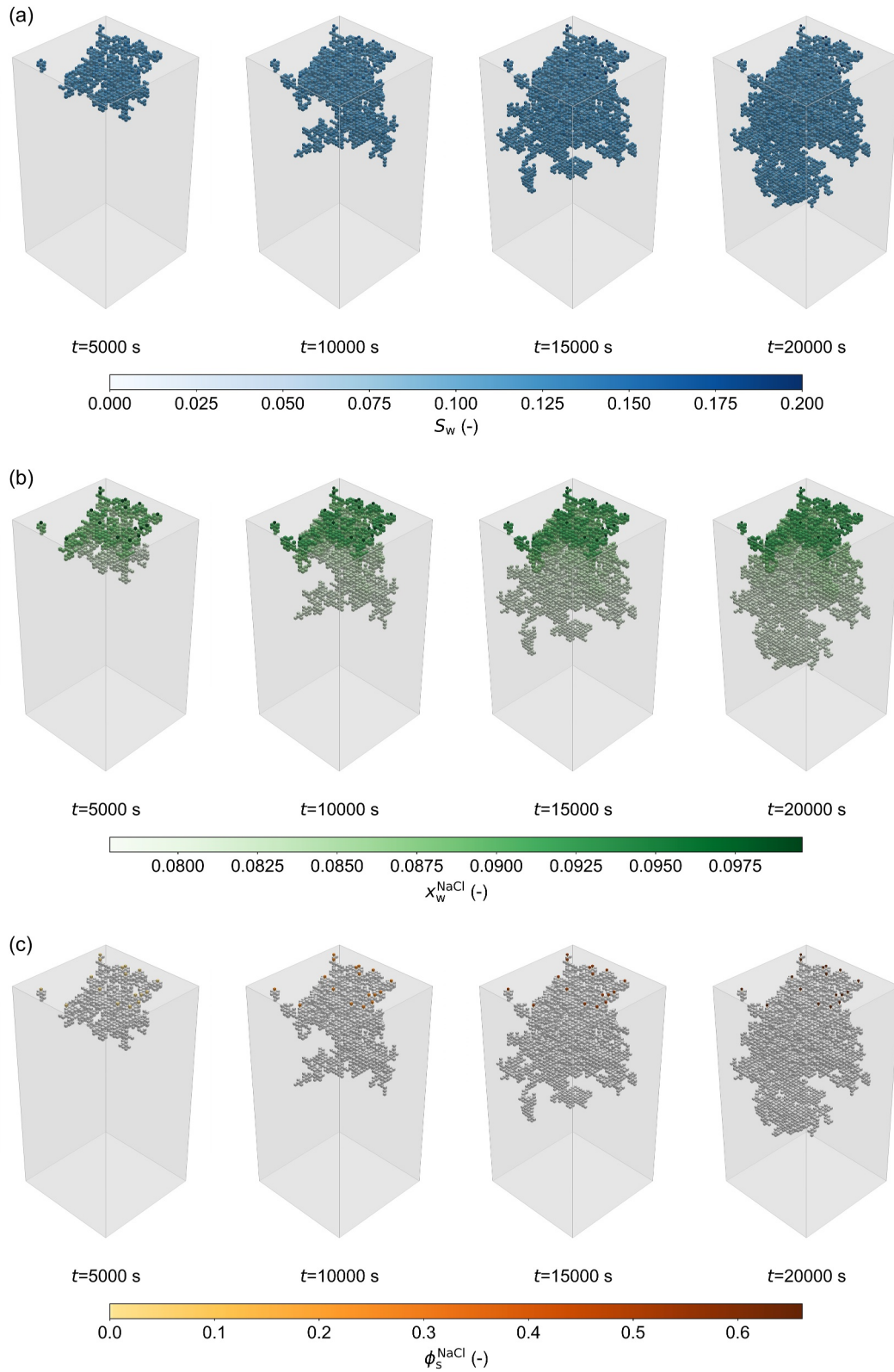

Figure 15. Temporal evolution of (a) liquid-phase saturation, (b) dissolved-salt concentration, and (c) precipitated-salt distribution within the invaded cluster during brine evaporation in PN4.

during an instantaneous liquid phase redistribution. The proposed QSPNM was compared against a fully implicit DPNM for pure water and brine evaporation in one-, two-, and three-dimensional pore networks. The numerical convergence of the QSPNM was evaluated using four different time step sizes. Furthermore, the computational performance of each sub-process was quantitatively evaluated, and the average wall-clock time per time step was compared with that of the DPNM. Finally, the enhanced computational capacity of the framework was demonstrated through the simulation of pure water and brine evaporation in a large pore network. The main findings are summarized below.

The proposed QSPNM captures salt migration through continuous corner liquid in invaded regions. This hydraulic connectivity provides the dominant pathway for salt advection from the interior to the evaporating surface, which is critical for predicting realistic precipitation patterns. The QSPNM accurately reproduces the temporal evolution of the liquid saturation fields, salt concentration distributions, and precipitated salt patterns computed from the DPNM. For all benchmark cases, the volume-weighted spatio-temporal absolute L^2 errors remain below 0.02 for all quantities. The time-integrated liquid flux approximation was also validated, resulting in median relative errors below 1% in 1D networks and below 10% in higher-dimensional networks when using the post-invasion throat conductance.

The QSPNM demonstrates substantially improved numerical robustness and convergence compared to the DPNM. The dynamic model exhibits convergence difficulties in heterogeneous pore networks, where large time steps fail to resolve invasions in throats with near-identical entry pressures, leading to erroneous invasion sequences. In contrast, the QSPNM remains stable and convergent across all cases, even with time steps up to 1 s. This robustness stems from the physical assumption of instantaneous liquid redistribution and the use of a fully implicit scheme for salt transport.

The decoupled solution strategy of the QSPNM leads to significant computational savings. Compared to the DPNM, the QSPNM is 6.9–18.6 times faster per time step for pure water evaporation and 5.5–13.6 times faster for brine evaporation. A performance analysis of the QSPNM shows that liquid redistribution is the most computationally expensive step in pure water cases, accounting for 76%–78% of the cost. In brine simulations, the computational cost is dominated by two primary components: liquid redistribution (36%–43.5%) and the salt transport/precipitation calculations (34.5%–40%). The successful simulation of evaporation of pure water and brine in a large pore network confirms the computational capability and practical applicability of the QSPNM to realistic porous media.

Overall, the proposed QSPNM delivers a substantial improvement in computational efficiency over the DPNM by enabling much larger time steps while requiring significantly less wall-clock time per time step. Despite this efficiency gain, the QSPNM achieves accuracy comparable to that of the DPNM, making it a reliable and highly efficient alternative for simulating evaporation-driven salt transport and precipitation in capillary-dominated regimes. By preserving the essential pore-scale physics at a significantly reduced computational cost, the framework is well-suited for systematic parameter studies and uncertainty analyses on larger pore networks. These results also provide practical guidance for model selection: the DPNM is preferable for studies that require detailed resolution of transient invasion dynamics, whereas the proposed QSPNM is a more efficient and robust choice for capillary-dominated, long-duration simulations on larger pore networks. This capability provides a robust, pore-scale foundation for developing improved constitutive relationships and upscaling strategies for REV-scale descriptions of evaporation-driven salt precipitation in porous media.

Conflict of Interest

The authors declare no conflicts of interest relevant to this study.

Availability Statement

Simulation data used in this study are openly available in the DaRUS repository (Z. Chen, 2026): https://doi.org/10.18419/DARUS-6130. These include "vtp" files containing all simulation outputs, as well as the processed Excel data sets used for figure generation and analysis. The quasi-static pore-network model developed in this study is described in full in Section 2, and its complete computational procedure is provided as Algorithm S1 in the Supporting Information S1; together with the archived data set, this information is sufficient to reproduce the

results reported here. The fully implicit dynamic pore-network model used for comparison is that of Schollenberger et al. (2025). Figures were created using Python. All input data, outputs, and scripts used for plotting figures are included in the DaRUS archive.

Acknowledgments
All authors acknowledge funding from the Deutsche Forschungsgemeinschaft (DFG, German Research Foundation) through the Collaborative Research Center SFB 1313 (Project No. 327154368). B. Guo acknowledges support from a Humboldt Research Fellowship for Experienced Researchers from the Alexander von Humboldt Foundation, and Z. Chen acknowledges support from a Humboldt Research Fellowship for Postdoctoral Researchers from the Alexander von Humboldt Foundation. Open Access funding enabled and organized by Projekt DEAL.

References

Ahmad, F., Rahimi, A., Tsotsas, E., Prat, M., & Kharaghani, A. (2021). From micro-scale to macro-scale modeling of solute transport in drying capillary porous media. *International Journal of Heat and Mass Transfer*, *165*, 120722. https://doi.org/10.1016/j.ijheatmasstransfer.2020.120722

Bakke, S., & Øren, P.-E. (1997). 3-D pore-scale modelling of sandstones and flow simulations in the pore networks. *SPE Journal*, *2*(2), 136–149. https://doi.org/10.2118/35479-PA

Biswas, S., Fantinel, P., Borgman, O., Holtzman, R., & Goehring, L. (2018). Drying and percolation in correlated porous media. *Physical Review Fluids*, *3*(12), 124307. https://doi.org/10.1103/PhysRevFluids.3.124307

Borgman, O., Fantinel, P., Lühder, W., Goehring, L., & Holtzman, R. (2017). Impact of spatially correlated pore-scale heterogeneity on drying porous media. *Water Resources Research*, *53*(7), 5645–5658. https://doi.org/10.1002/2016WR020260

Bringedal, C., Schollenberger, T., Pieters, G. J. M., Van Duijn, C. J., & Helmig, R. (2022). Evaporation-Driven density instabilities in saturated porous media. *Transport in Porous Media*, *143*(2), 297–341. https://doi.org/10.1007/s11242-022-01772-w

Chaudhry, M. A., Kiemle, S., Pohlmeier, A., Helmig, R., & Huisman, J. A. (2026). Non-Invasive imaging of solute redistribution below evaporating surfaces Using ^{23}Na-MRI. *Water Resources Research*, *62*(1), e2025WR041207. https://doi.org/10.1029/2025WR041207

Chen, S., Qin, C., & Guo, B. (2020). Fully implicit dynamic pore-network modeling of two-phase flow and phase change in porous media. *Water Resources Research*, *56*(11), e2020WR028510. https://doi.org/10.1029/2020WR028510

Chen, Z. (2026). Replication data for quasi-static pore-network modeling for evaporation-driven salt transport and precipitation in porous media [dataset]. *DaRUS*. https://doi.org/10.18419/DARUS-6130

Chen, Z., Helmig, R., & Hu, L. (2025). Heat and moisture migration in porous media during remediation using superheated steam injection: A coupled experimental and numerical study. *Physics of Fluids*, *37*(4). https://doi.org/10.1063/5.0262877

Chen, Z., Helmig, R., & Hu, L. (2026). Numerical investigation of multiphase contaminant removal from NAPL-impacted soils: A comparative study of thermal desorption approaches. *Journal of Contaminant Hydrology*, *278*, 104888. https://doi.org/10.1016/j.jconhyd.2026.104888

Cui, G., Hu, Z., Ning, F., Jiang, S., & Wang, R. (2023). A review of salt precipitation during CO2 injection into saline aquifers and its potential impact on carbon sequestration projects in China. *Fuel*, *334*, 126615. https://doi.org/10.1016/j.fuel.2022.126615

Dashtian, H., Shokri, N., & Sahimi, M. (2018). Pore-network model of evaporation-induced salt precipitation in porous media: The effect of correlations and heterogeneity. *Advances in Water Resources*, *112*, 59–71. https://doi.org/10.1016/j.advwatres.2017.12.004

Doehne, E. (2002). Salt weathering: A selective review. *Geological Society, London, Special Publications*, *205*(1), 51–64. https://doi.org/10.1144/GSL.SP.2002.205.01.05

Guo, Y., Jiang, F., Tsuji, T., Kato, Y., Shimokawara, M., Esteban, L., et al. (2026). Machine learning-based upscaling of rock permeability from pore scale to core scale: Effect of training dataset size and sub-core volumes. *Earth Energy Science*, *2*(1), 100041. https://doi.org/10.1016/j.ees.2025.11.008

Jambhekar, V. A., Helmig, R., Schröder, N., & Shokri, N. (2015). Free-flow–porous-media coupling for evaporation-driven transport and precipitation of salt in soil. *Transport in Porous Media*, *110*(2), 251–280. https://doi.org/10.1007/s11242-015-0516-7

Jambhekar, V. A., Mejri, E., Schröder, N., Helmig, R., & Shokri, N. (2016). Kinetic approach to model reactive transport and mixed salt precipitation in a coupled free-flow–Porous-Media system. *Transport in Porous Media*, *114*(2), 341–369. https://doi.org/10.1007/s11242-016-0665-3

Joekar-Niasar, V., Hassanizadeh, S. M., & Dahle, H. K. (2010). Non-equilibrium effects in capillarity and interfacial area in two-phase flow: Dynamic pore-network modelling. *Journal of Fluid Mechanics*, *655*, 38–71. https://doi.org/10.1017/S0022112010000704

Joekar-Niasar, V., Hassanizadeh, S. M., & Leijnse, A. (2008). Insights into the relationships among capillary pressure, saturation, interfacial area and relative permeability using pore-network modeling. *Transport in Porous Media*, *74*(2), 201–219. https://doi.org/10.1007/s11242-007-9191-7

Lehmann, P., Assouline, S., & Or, D. (2008). Characteristic lengths affecting evaporative drying of porous media. *Physical Review E*, *77*(5), 056309. https://doi.org/10.1103/PhysRevE.77.056309

Lenormand, R., Touboul, E., & Zarcone, C. (1988). Numerical models and experiments on immiscible displacements in porous media. *Journal of Fluid Mechanics*, *189*, 165–187. https://doi.org/10.1017/S0022112088000953

Nowicki, S. C., Davis, H. T., & Scriven, L. E. (1992). Microscopic determination of transport paraheters in drying porous media. *Drying Technology*, *10*(4), 925–946. https://doi.org/10.1080/07373939208916488

Øren, P., Bakke, S., & Arntzen, O. (1998). Extending predictive capabilities to network models. *SPE Journal*, *3*(4), 324–336. https://doi.org/10.2118/52052-PA

Patzek, T., & Silin, D. (2001). Shape factor and hydraulic conductance in noncircular capillaries. *Journal of Colloid and Interface Science*, *236*(2), 295–304. https://doi.org/10.1006/jcis.2000.7413

Prat, M. (1993). Percolation model of drying under isothermal conditions in porous media. *International Journal of Multiphase Flow*, *19*(4), 691–704. https://doi.org/10.1016/0301-9322(93)90096-D

Prat, M. (2007). On the influence of pore shape, contact angle and film flows on drying of capillary porous media. *International Journal of Heat and Mass Transfer*, *50*(7–8), 1455–1468. https://doi.org/10.1016/j.ijheatmasstransfer.2006.09.001

Ransohoff, T., & Radke, C. (1988). Laminar flow of a wetting liquid along the corners of a predominantly gas-occupied noncircular pore. *Journal of Colloid and Interface Science*, *121*(2), 392–401. https://doi.org/10.1016/0021-9797(88)90442-0

Roy, R., Weibel, J. A., & Garimella, S. V. (2022). Modeling the formation of efflorescence and subflorescence caused by salt solution evaporation from porous media. *International Journal of Heat and Mass Transfer*, *189*, 122645. https://doi.org/10.1016/j.ijheatmasstransfer.2022.122645

Schneider, M., Wu, H., Veyskarami, M., Pop, S., & Helmig, R. (2025). Improvement of fully-implicit two-phase pore-network models by employing generalized flux functions with additional throat variables (No. arXiv:2504.01529). *arXiv*. https://doi.org/10.48550/arXiv.2504.01529

Schollenberger, T., Rohde, C., & Helmig, R. (2025). Two-phase pore-network model for evaporation-driven salt precipitation – Representation and analysis of pore-scale processes. *arXiv*. (No. arXiv:2503.22533). https://doi.org/10.48550/arXiv.2503.22533

Schollenberger, T., Von Wolff, L., Bringedal, C., Pop, I. S., Rohde, C., & Helmig, R. (2024). Investigation of different throat concepts for precipitation processes in saturated pore-network models. *Transport in Porous Media*, *151*(14), 2647–2692. https://doi.org/10.1007/s11242-024-02125-5

Shahraeeni, E., Lehmann, P., & Or, D. (2012). Coupling of evaporative fluxes from drying porous surfaces with air boundary layer: Characteristics of evaporation from discrete pores. *Water Resources Research*, *48*(9), 2012WR011857. https://doi.org/10.1029/2012WR011857

Shokri, N., Hassani, A., & Sahimi, M. (2024). Multi-scale soil salinization dynamics from global to pore scale: A review. *Reviews of Geophysics*, *62*(4), e2023RG000804. https://doi.org/10.1029/2023RG000804

Shokri, N., Rutner, M., Kang, B., Rutner, M., & Smarsly, K. (2026). Climate-informed engineering for subsurface management: Concept, framework, and applications. *Earth Energy Science*, *2*(2), 100055. https://doi.org/10.1016/j.ees.2026.100055

Surasani, V. K., Metzger, T., & Tsotsas, E. (2010). Drying simulations of various 3D pore structures by a nonisothermal pore network model. *Drying Technology*, *28*(5), 615–623. https://doi.org/10.1080/07373931003788676

Veran-Tissoires, S., & Prat, M. (2014). Evaporation of a sodium chloride solution from a saturated porous medium with efflorescence formation. *Journal of Fluid Mechanics*, *749*, 701–749. https://doi.org/10.1017/jfm.2014.247

Wan, J., & Tokunaga, T. K. (1997). Method of measuring contact angle on spheres. *Journal of Colloid and Interface Science*, *189*(1), 186–190. https://doi.org/10.1006/jcis.1997.4822

Wang, Y., & Hu, L. (2023). A theoretical model of soil freezing characteristic curve considering the freezing of adsorbed water and capillary water. *Water Resources Research*, *59*(7), e2023WR034662. https://doi.org/10.1029/2023wr034662

Wang, Y., Hu, L., Luo, S., & Lu, N. (2022). Soil water isotherm model for particle surface sorption and interlamellar sorption. *Vadose Zone Journal*, *21*(5). https://doi.org/10.1002/vzj2.20221

Wang, Y., Wu, Y., Hu, L., Hicher, P.-Y., & Yin, Z.-Y. (2025). A hydraulic conductivity model incorporating adsorption and capillarity for unsaturated/frozen soil. *Engineering Geology*, *353*, 108093. https://doi.org/10.1016/j.enggeo.2025.108093

Weishaupt, K., & Helmig, R. (2021). A dynamic and fully implicit non-isothermal, two-phase, two-component pore-network model coupled to single-phase free flow for the pore-scale description of evaporation processes. *Water Resources Research*, *57*(4), e2020WR028772. https://doi.org/10.1029/2020WR028772

Weishaupt, K., Koch, T., & Helmig, R. (2022). A fully implicit coupled pore-network/free-flow model for the pore-scale simulation of drying processes. *Drying Technology*, *40*(4), 697–718. https://doi.org/10.1080/07373937.2021.1955706

Wu, H., Veyskarami, M., Schneider, M., & Helmig, R. (2023). A new fully implicit two-phase pore-network model by utilizing regularization strategies. *Transport in Porous Media*, *151*(1), 1–26. https://doi.org/10.1007/s11242-023-02031-2

Wu, R., & Chen, F. (2023). Interplay between salt precipitation, corner liquid film flow, and gas–liquid displacement during evaporation in microfluidic pore networks. *Journal of Applied Physics*, *133*(7), 074701. https://doi.org/10.1063/5.0135135

Wu, R., Zhang, T., Ye, C., Zhao, C. Y., Tsotsas, E., & Kharaghani, A. (2020). Pore network model of evaporation in porous media with continuous and discontinuous corner films. *Physical Review Fluids*, *5*(1), 014307. https://doi.org/10.1103/PhysRevFluids.5.014307

Wu, R., & Zhao, C. Y. (2021). Distribution of liquid flow in a pore network during evaporation. *Physical Review E*, *104*(2), 025107. https://doi.org/10.1103/PhysRevE.104.025107

Xiong, Q. X., & Meftah, F. (2021). Determination on pore size distribution by a probabilistic porous network subjected to salt precipitation and dissolution. *Computational Materials Science*, *195*, 110491. https://doi.org/10.1016/j.commatsci.2021.110491

Yang, J., Lei, T., Wang, G., Xu, Q., Chen, J., & Luo, K. H. (2023). Lattice boltzmann modelling of salt precipitation during brine evaporation. *Advances in Water Resources*, *180*, 104542. https://doi.org/10.1016/j.advwatres.2023.104542

Yang, Z., Li, D., Zhu, Y., Zhu, X., Yu, W., Yang, K., & Chen, B. (2024). Developing salt-rejecting evaporators for solar desalination: A critical review. *Environmental Science & Technology*, *58*(20), 8610–8630. https://doi.org/10.1021/acs.est.3c09703

Yiotis, A. G., Boudouvis, A. G., Stubos, A. K., Tsimpanogiannis, I. N., & Yortsos, Y. C. (2004). Effect of liquid films on the drying of porous media. *AIChE Journal*, *50*(11), 2721–2737. https://doi.org/10.1002/aic.10265

Yiotis, A. G., Stubos, A. K., Boudouvis, A. G., Tsimpanogiannis, I. N., & Yortsos, Y. C. (2005). Pore-Network modeling of isothermal drying in porous media. *Transport in Porous Media*, *58*(1–2), 63–86. https://doi.org/10.1007/s11242-004-5470-8

Yiotis, A. G., Tsimpanogiannis, I. N., Stubos, A. K., & Yortsos, Y. C. (2007). Coupling between external and internal mass transfer during drying of a porous medium. *Water Resources Research*, *43*(6), 2006WR005558. https://doi.org/10.1029/2006WR005558

Zhang, C., Li, L., & Lockington, D. (2014). Numerical study of evaporation-induced salt accumulation and precipitation in bare saline soils: Mechanism and feedback. *Water Resources Research*, *50*(10), 8084–8106. https://doi.org/10.1002/2013WR015127

Zhang, H., Sun, Z., Zhang, N., & Zhao, B. (2024). Brine drying and salt precipitation in porous media: A microfluidics study. *Water Resources Research*, *60*(1), e2023WR035670. https://doi.org/10.1029/2023WR035670

Zhou, D., Blunt, M., & Orr, F. (1997). Hydrocarbon drainage along corners of noncircular capillaries. *Journal of Colloid and Interface Science*, *187*(1), 11–21. https://doi.org/10.1006/jcis.1996.4699